The inflated radii of M-dwarfs in the Pleiades

R. J. Jackson[1], Constantine P. Deliyannis[2] and R. D. Jeffries[1]
[1] *Astrophysics Group, Keele University, Keele, Staffordshire ST5 5BG*
[2]*Department of Astronomy, Indiana University. 727 E 3rd Street, Bloomington, IN 47405-7105, USA*

Submitted

ABSTRACT
Rotation periods obtained with the Kepler satellite have been combined with precise measurements of projected rotation velocity from the WIYN 3.5-m telescope to determine the distribution of projected radii for several hundred low-mass ($0.1 \leqslant M/M_{\odot} \leqslant 0.8$), fast-rotating members of the Pleiades cluster. A maximum likelihood modelling technique, that takes account of observational uncertainties, selection effects and censored data, and considers the effects of differential rotation and unresolved binarity, has been used to find that the average radius of these stars is 14 ± 2 per cent larger at a given luminosity than predicted by the evolutionary models of Dotter et al. (2008) and Baraffe et al. (2015). The same models are a reasonable match to the interferometric radii of older, magnetically inactive field M-dwarfs, suggesting that the over-radius may be associated with the young, magnetically active nature of the Pleiades objects. No evidence is found for any change in this over-radius above and below the boundary marking the transition to full convection. Published evolutionary models that incorporate either the effects of magnetic inhibition of convection or the blocking of flux by dark starspots do not individually explain the radius inflation, but a combination of the two effects might. The distribution of projected radii is consistent with the adopted hypothesis of a random spatial orientation of spin axes; strong alignments of the spin vectors into cones with an opening semi-angle $< 30^{\circ}$ can be ruled out. Any plausible but weaker alignment would increase the inferred over-radius.

Key words: stars: magnetic activity; stars: low-mass – stars: evolution – stars: pre-main-sequence – clusters and associations: general – starspots

1 INTRODUCTION

The radii of tidally-locked, main-sequence K- and M-dwarfs in eclipsing binary systems are consistently measured to be larger than predicted by most evolutionary models. The radius discrepancies amount to 10–20 per cent at a fixed mass and thus for a fixed luminosity, the effective temperature, $T_{\rm eff}$, can be underestimated by 5–10 per cent (e.g. Lopez-Morales & Ribas 2005; Morales et al. 2009; Torres 2013). The tidally-locked components of these binary systems are fast-rotating and magnetically active; this, together with the fact that interferometrically measured radii for nearby, relatively inactive K- and M-dwarfs are in much better agreement with models (e.g. Demory et al. 2009; Boyajian et al. 2012), has led to theoretical developments that explain "radius inflation" in terms of the effects of dynamo-generated magnetic activity (Morales, Ribas & Jordi 2008).

Magnetic activity might have an influence on the radii of cool, convective stars either through inhibition of convection throughout the star (Mullan & MacDonald 2001; Feiden & Chaboyer 2014) or by blocking the emergence of radiative flux at the photosphere with dark, magnetic starspots (e.g. Spruit & Weiss 1986; MacDonald & Mullan 2013; Jackson & Jeffries 2014a). Young stars on the pre-main-sequence (PMS) or at the zero-age main sequence (ZAMS) are also highly magnetically active as a consequence of their rapid rotation. If magnetic activity is responsible for inflating the radii of fast-rotating binary components, then it seems likely that the same phenomenon will be exhibited by low-mass PMS and ZAMS stars.

Substantial evidence has emerged that this is the case. Inflated radii have been invoked to explain a number of puzzles: the rotation-dependent anomalous colours of PMS and ZAMS stars (Stauffer et al. 2003; Kamai et al. 2014; Covey et al. 2016); the rotation-dependent scatter of lithium depletion seen among PMS and ZAMS stars of similar mass and age (e.g. Somers & Pinsonneault 2014, 2015a,b) and the discrepancies between model predictions and the measured masses, radii and luminosities of PMS and ZAMS eclipsing binary systems (Kraus et al. 2015, 2016; David et al. 2016). The adoption of "magnetic models" for low-mass stars leads to the inference of significantly older ages (by a factor of two) and higher masses for PMS stars (Feiden 2016; Messina et al. 2016; Jeffries et al. 2017) from the Hertzsprung-Russell diagram and commensurately longer empirically determined timescales for the duration of star and planet formation.

Ideally, testing PMS/ZAMS magnetic models would involve direct measurements of stellar masses and radii, but these are only directly accessible for binary stars that might also be affected by tidal locking. Even the nearest PMS/ZAMS stars are just too far away for precise interferometric radius determinations. Indirect es-

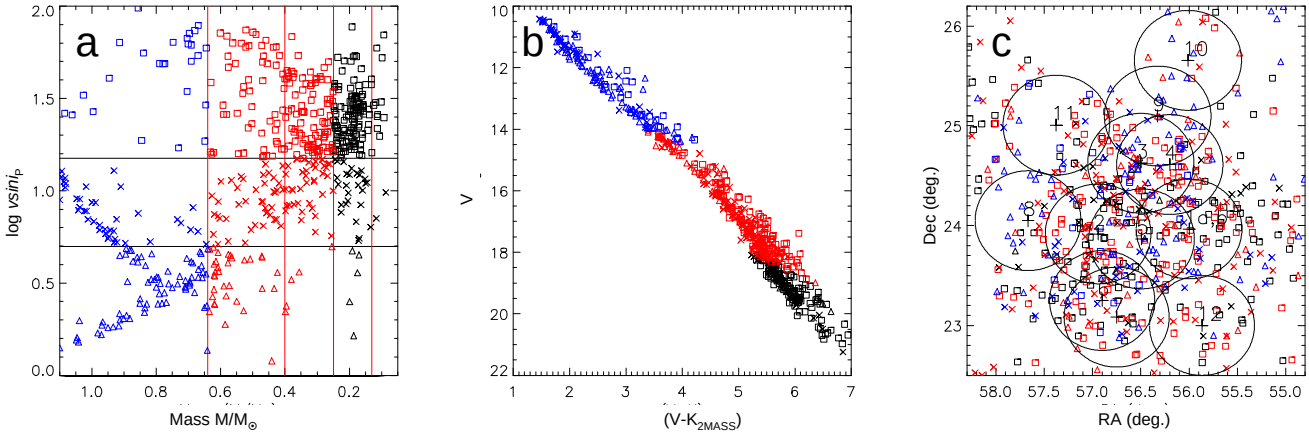

Figure 1. Target selection: panel (a) shows $(v \sin i)_p$ as a function of estimated mass (see section 2.1) for low mass stars in the Peiades with measured period. Symbols correspond to the predicted observed $(v \sin i)_p$ (for an average spin-axis inclination and no radius inflation; triangles indicate $(v \sin i)_p < 5$ km s^{-1}, crosses have $5 < (v \sin i)_p < 15$ km s^{-1} and squares $(v \sin i)_p \geqslant 15$ km s^{-1}), whilst the different colours correspond to intervals in mass inferred from the observed $K_{\rm 2MASS}$ magnitude and $V-K$ colour (blue for $M > 0.64 M_\odot$, red for $0.64 > M/M_\odot > 0.25$ and black for $M < 0.25 M_\odot$. Panel (b) shows V versus $V - K_{\rm 2MASS}$ colour magnitude diagram for the same data set using the same symbols and colour coding. Panel (c) shows spatial distribution of low mass targets in the central region of the Pleiades. The large circles show the fields of view of the twelve observed WIYN Hydra configurations (see Table 1).

timates of stellar radii can be made from measured luminosities and $T_{\rm eff}$ determined from colours or spectroscopy. This approach was adopted by Somers & Stassun (2017) in the Pleiades cluster (age 120 Myr) and they found some evidence for inflated radii (by 10–30 per cent) in ZAMS K-stars with rotation periods < 2 days compared with slower rotating stars of similar spectral type. Unfortunately this technique is subject to systematic errors in the $T_{\rm eff}$ estimation and is insensitive to any inflation caused by dark starspots, since these can reduce the luminosity of a star whilst leaving the colour and spectral type largely unchanged.

An alternative geometric technique is to use the product of rotation period (P in days) with projected equatorial velocity ($v \sin i$ in km s^{-1}), which yields the *projected* stellar radius, in solar units;

$$R \sin i = 0.0198 \, P \, v \sin i \qquad (1)$$

(e.g. Rhode, Herbst & Mathieu 2001; Jeffries 2007). By assuming a random spin axis orientation (e.g. Jackson & Jeffries 2010a) and taking account of observational biases, a set of $R \sin i$ estimates can be modelled to determine the true average radius for a group of stars, with a precision that improves with larger samples.

The $P \, v \sin i$ method was used by Hartman et al. (2010) to estimate average radii for G- and K-stars in the Pleiades using rotation periods from the HATNet survey and $v \sin i$ measurements from a variety of literature sources. They concluded that stars with $M \geqslant 0.85 M_\odot$ have radii consistent with non-magnetic evolutionary models, but that stars with $0.6 < M/M_\odot < 0.85$ were 10 per cent larger than predicted. Jackson & Jeffries (2014a) used the same dataset and a similar modelling technique to compare the radii of Pleiades stars with $0.55 \leqslant M/M_\odot < 1.0$ with the interferometric radii of inactive main sequence field stars, finding an over-radius of 13 ± 3 per cent. Lanzafame et al. (2017) performed their own analysis showing that the effect appears to be driven by a ~ 30 per cent inflation for a subset of stars with $0.6 < M/M_\odot < 0.8$ that are intermediate in rotation rate, but that faster rotators or more massive stars have radii consistent with model predictions.

The goal of the present study is to extend these studies in the Pleiades to lower masses. The motivation is twofold. First, Jackson et al. (2009) and Jackson & Jeffries (2014a) applied these techniques to M-dwarfs in NGC 2516, a cluster with a similar age to the Pleiades, finding a dramatic radius inflation that increased with decreasing mass, reaching ~ 40 per cent for the lowest masses considered ($\simeq 0.25 M_\odot$). Whilst a number of systematic effects (differential rotation, binarity) have been considered and accounted for, it is *possible* that the rotation periods used, which were based on a relatively short ground-based campaign, might have led to a mistaken upward bias. The result has however been supported (with low precision) by measurements of a few M-dwarfs in an even younger cluster (NGC 2547, Jackson et al. 2016), but we wish to confirm whether such large radius increases are present in a larger sample with better-determined periods (see below). Second, the predictions of the different flavours of magnetic model differ for low-mass stars that are mostly or fully convective. Magnetic inhibition of convection predicts a stronger effect in higher mass stars with large radiative cores (Feiden & Chaboyer 2015), whereas inflation due to starspots is predicted to be more effective in fully convective stars, especially those which have yet to reach the ZAMS, which is the case for stars with $M < 0.4 M_\odot$ at the age of the Pleiades (Jackson & Jeffries 2014a). Hence measurements of radius inflation across the "fully convective boundary" could be diagnostic of the mechanism by which radius inflation occurs.

In this paper we present new results for low-mass stars in the Pleiades. The cluster was included in the Kepler K2 mission (Howell et al. 2014) for 72 days during "campaign 4", starting 8th February 2015. Rebull et al. (2016a) reported 760 rotation periods for low-mass stars, including ~ 600 in the range $0.1 < M/M_\odot < 0.9$. To this can be added a further 40 periods for low mass stars ($\leqslant 0.45 M_\odot$) from the Palomar Transit Factory survey (Covey et al. 2016), and together these provide a large catalogue of reliable rotation periods that bridge the fully convective boundary.

We have targeted these objects with fibre spectroscopy from the WIYN[1] 3.5-m telescope at the Kitt Peak National Observatory, in order to determine $v \sin i$ and hence distributions of $R \sin i$. In

[1] The WIYN Observatory is a joint facility of the University of Wisconsin

sections 2 and 3 we describe the target selection and the measurements that were made at the WIYN telescope. Sections 4 and 5 describe the analysis of these spectra to determine $v \sin i$ for individual objects and to determine the average over-radius for groups of objects. In section 6 we discuss the significance of our results and compare them with the predictions of non-magnetic models and models that include the effects of magnetic inhibition of convection and starspots. Section 7 contains our conclusions.

2 SPECTROSCOPIC OBSERVATIONS

2.1 Target selection

Potential targets were selected from lists of Pleiades members with measured periods reported by Rebull et al. (2016a), Covey et al. (2016) and Hartman et al. (2010). Rotation period data were taken preferentially from Rebull et al. (705 targets), then from Covey el al. (44) and lastly from Hartman et al. (64). Data were matched with the 2MASS catalogue (Skrutskie el al. 2006) to give target co-ordinates (RA and Dec) and the apparent $K_{\rm 2MASS}$ magnitude. Figure 1 shows the distribution of potential targets in RA and Dec and in the colour-magnitude diagram. Targets for our fiber-spectroscopy study were selected from a 10 square degrees with the highest target density.

The targets were prioritised according to their mass, M (highest priority was given to lowest masses, but with a practical faint magnitude limit of $I = 17.3$), and a prediction of their observed projected equatorial velocity, $(v \sin i)_p = (\pi/4) 50\, R/P$ in $\mathrm{km\,s^{-1}}$, where P is the rotation period in days and R is the estimated stellar radius in solar units. Masses and radii were estimated by comparing the luminosity of the potential target with the predictions of a 120 Myr solar metallicity, *non-magnetic* model isochrone from Baraffe et al. (2015) (hereafter BHAC15). The factor of $\pi/4$ is the mean value of $\sin i$, based on a crude assumption of an unbiased, random distribution of rotation axis orientations. The adopted metallicity and age are consistent with [Fe/H]$= 0.03 \pm 0.05$ reported by Soderblom et al. (2009) and the lithium depletion boundary age of 125 ± 8 Myr given by Stauffer, Schultz & Kirkpatrick (1998). The luminosity of each source was estimated from its M_K value (accounting for extinction and distance, see below) using a bolometric correction calculated using $(V-K)_0$ and the BHAC15 models. An intrinsic distance modulus of 5.67 ± 0.02 mag was assumed (Melis et al. 2014), a conversion of $K_{\rm CIT} = K_{\rm 2MASS} + 0.024$ (Carpenter 2001) and a reddening of $E(B-V) = 0.032$ mag (An, Terndrup & Pinsonneault 2007). Using the relations of Rieke & Lebofsky (1985) this reddening corresponds to extinction of $A_V = 0.10$ mag and $A_K = 0.01$ mag.

The targets were binned according to $(v \sin i)_p$ (see Fig. 1a). Highest priority was given to the faster rotating targets with $(v \sin i)_p \geqslant 15 \mathrm{km\,s^{-1}}$, which are expected to yield measurable $v \sin i$ values at the resolution of the spectroscopic data (see section 2.2). Second priority was given to targets with $(v \sin i)_p \leqslant 5\,\mathrm{km\,s^{-1}}$ to provide a sample of very slow rotators which are expected to have unbroadened spectral lines and serve as a baseline for calibrating the measured $v \sin i$ as a function of spectral line width broadening (see section 3.4).

Madison, Indiana University, the National Optical Astronomy Observatory and the University of Missouri.

2.2 Observations

The WIYN Hydra multi-object spectrograph (Bershady et al. 2008) consists of a robotic positioner that can position up to 83 fibres, each with a 3 arcsecond diameter (we used the "blue" fibre cable), across a 1 degree diameter unvignetted field of view at the Nasmyth focus of the 3.5-m WIYN telescope. The fibers were used in conjunction with the bench spectrograph, an echelle grating and an order-sorting filter to provide spectra with a resolving power of $\simeq 17,000$. An STA1 2600×4000 pixel CCD camera was used in 2×2 binning mode to record spectra covering ~ 400Å centred at ~ 7850Å. The FWHM of a resolution element corresponded to about 2.5 binned pixels. Twelve field centres were chosen to maximise the number of high priority targets (see section 2.1). Spare fibres were allocated to second priority targets and to repeat observations of targets in cases of over-lap between fields. Finally, ∼20 spare fibres were allocated to clear sky >20 arcsec away from the nearest source in the 2MASS catalogue.

The observing program was performed over 9 nights during a 6 month period from September 2016 to February 2017, although poor weather restricted the total observing time available. Details of when each of the twelve fields was observed (field 1 was observed on two nights), how many targets were in each field and how long the fields were exposed for are given in Table 1. The range in apparent I magnitude (the relevant magnitude for the wavelength at which we observed) within a particular configuration was restricted to < 5 magnitudes to limit any cross-contamination of spectra between adjacent fibres. To make best use of varying observing conditions we further divided the targets into "bright" and "faint" samples (with overlap). For configurations of fainter targets ($12.3 < I < 17.3$), several one hour exposures were required to produce sufficient signal to noise (SNR) in the spectra to allow resolution of $v \sin i$ in the faintest targets. The brighter targets ($9 < I < 14$) required less time and could be observed more readily in partially cloudy skies. The names, co-ordinates, photometry, rotation periods, estimated masses and radii (from the BHAC15 models) and derived luminosities for the 324 individual Pleiades targets that were actually observed are listed in Table 2.

2.3 Additional observations of slowly rotating stars

There were an insufficient number of slow-rotating M-dwarfs in the Pleiades to adequately characterise the width of spectral lines in stars with negligible rotational broadening (see section 3.4). To that end, also listed at the end of Table 2, are 88 low-mass targets from Praesepe, an older cluster, which also has measured periods based on K2 observations (Douglas et al. 2017) and which contains a higher proportion of slow-rotating M dwarfs ($(v \sin i)_p \leqslant 3\,\mathrm{km\,s^{-1}}$). The spectra of these stars were observed on the same nights as the Pleiades targets and with exactly the same Hydra spectrograph set up and were taken from a comprehensive set of observations made of low-mass Praesepe stars with known periods, which will be reported on in a subsequent paper. M_K values are estimated assuming a distance modulus of 6.29±0.07 mag (van Leeuwen 2009) and zero reddening. Stellar masses and radii were estimated from intrinsic $V-K$ colour and the BHAC15 models, assuming a cluster age of 670 Myr (e.g. Cummings et al. 2017).

Table 1. Hydra Configurations observed in the Pleiades. The positions are those of the field centres.

Config. number	File number	Range of I magnitude	Date	UT of exposure #1	RA (J2000)	Dec (J2000)	Exposure time (s)	Number exposures	Fibres on targets	Fibres on sky
1a	1013	12.3 to 17.3	2016-09-24	08:07:09	03:43:59.99	23:57:59.94	3600	3	48	27
1b	2046	12.3 to 17.3	2016-09-25	07:59:09	03:43:59.99	23:57:59.94	3600	4	48	27
2	4054	12.3 to 17.3	2017-01-03	05:43:01	03:47:46.00	23:55:00.08	3600	6	52	20
3	6063	12.3 to 17.3	2017-01-05	04:45:10	03:45:59.99	24:37:29.93	3600	5	45	26
4	12053	9.6 to 14.0	2017-01-17	05:34:48	03:44:47.99	24:36:44.96	600	6	22	20
5	13025	9.6 to 14.0	2017-01-18	07:11:14	03:45:58.00	23:52:00.01	600	6	22	28
6	14025	9.6 to 14.0	2017-01-19	02:03:00	03:47:35.99	23:14:59.98	3000	5	40	29
7	21063	9.6 to 14.0	2017-02-02	02:20:17	03:46:59.99	23:04:59.96	1200	3	30	25
8	21066	9.6 to 14.0	2017-02-02	03:47:40	03:50:39.99	24:03:00.06	1200	3	24	26
9	21075	9.6 to 14.0	2017-02-02	05:53:13	03:45:18.10	25:05:58.01	1200	3	22	25
10	22073	9.6 to 14.0	2017-02-03	02:25:01	03:44:02.79	25:39:22.08	1200	3	7	25
11	22076	9.6 to 14.0	2017-02-03	03:51:08	03:49:30.00	25:00:30.05	1200	3	18	26
12	22079	12.3 to 17.3	2017-02-03	05:19:13	03:43:27.99	23:00:00.05	3600	2	33	25

Table 2. Properties of observed science targets in the Pleiades and reference slow rotators in Praesepe. Masses and radii are estimated from the models of BHAC15. The final column gives the predicted equatorial velocity – see section 2.1. A sample of the table is given here, the full table is made available electronically.

Target name (2MASS)	RA (J2000)	Dec (J2000)	$K_{2\mathrm{MASS}}$ (mag)	$V-K$ (mag)	Period P (days)	Ref. *	BC_K (mag)	$\log L/L_\odot$	$M/M_\odot$	$R/R_\odot$	$(v \sin i)_p$ (km s^{-1})
J03414895+2303235	03 41 48.951	+23 03 23.54	13.19	6.09	0.239	1	2.86	-2.26	0.19	0.24	39.3
J03415671+2358434	03 41 56.716	+23 58 43.42	13.25	5.76	0.401	1	2.82	-2.27	0.18	0.24	23.3
J03415864+2257020	03 41 58.648	+22 57 02.00	11.90	4.78	6.842	1	2.72	-1.68	0.40	0.38	2.2
J03421789+2406578	03 42 17.890	+24 06 57.83	12.97	5.53	0.603	1	2.80	-2.15	0.22	0.26	17.0
J03422626+2351386	03 42 26.266	+23 51 38.67	13.45	5.97	0.496	1	2.85	-2.36	0.17	0.22	17.7
J03422941+2247261	03 42 29.418	+22 47 26.19	10.92	4.11	0.325	1	2.62	-1.25	0.56	0.52	62.4
J03423396+2411008	03 42 33.960	+24 11 00.81	13.42	5.89	0.564	1	2.84	-2.34	0.17	0.23	15.8
J03424184+2400158	03 42 41.848	+24 00 15.81	12.68	5.17	0.671	1	2.76	-2.01	0.26	0.29	17.1
J03424239+2320218	03 42 42.396	+23 20 21.87	11.45	5.28	0.269	1	2.77	-1.53	0.46	0.43	63.4

* Period measurement taken from (1) Rebull et al. 2016a, (2) Covey et al. 2016, (3) Hartman et al. 2010, (4) Douglas et al. 2017

3 DATA REDUCTION

Many of the target spectra were faint, requiring an optimal extraction strategy to provide sufficient signal-to-noise ratio (SNR) for useful analysis. Strong sky emission lines were a dominant feature in the fainter spectra. For these reasons we used purpose-built software for data reduction based on the pipeline described in Jackson & Jeffries (2010b), adapted where necessary, to the characteristics of the WIYN telescope and Hydra spectrograph.

3.1 Extraction of target spectra

Images of the science fields and associated flat and arc exposures were debiased and rebinned to compensate for the initial curvature of the spectra on the CCD image. The flat frames were the median of 11 tungsten-lamp flat exposures recorded in the afternoon prior to night-time observations. One dimensional spectra were optimally extracted from the science frames using the procedure described by Horne (1986). Counts per bin and uncertainties were calculated for a gain of 0.44 electrons/ADU and a read out noise of 3.1 electrons.

Arc spectra were extracted from Thorium-Argon lamp exposures recorded during the day prior to observations. Gaussian fits were used to determine the locations of 6 well-spaced unsaturated arc lines recorded through each fibre. Cubic polynomial fits to these were used to rebin spectra onto a common wavelength scale. The observations in September 2016 were centered on ∼7830Å with a common wavelength range of 7620–8035Å. Subsequent observations were centered on ∼7890Å with a common wavelength range of 7681–8095Å. A fine adjustment was made to the wavelength scale applied to each observation to compensate for drift between day-time calibration and night-time observations. The adjustment was determined by comparing the measured wavelength of six strong, unblended emission lines in the median sky spectra with their reported wavelengths. The weighted mean skyline correction varied from -0.6 to $+1.5$ km s^{-1} (-0.02Å to $+0.04$Å) with, in most cases, an uncertainty of $\leqslant 0.25$ km s^{-1} although a higher uncertainty (0.9 km s^{-1}) was found for configuration 5 (see Table 1).

Target spectra were sky subtracted using fibre efficiencies estimated from the amplitude of the flat field spectra which, when checked, showed good agreement (∼1.5 per cent rms) with the throughput measured from a twilight sky exposure of the same configuration on the same night. Spectra from repeated exposures in the same configuration (see Table 1) were corrected for heliocentric radial velocity and the median taken to produce final spectra, and corresponding uncertainties, in 0.1Å steps over the common wavelength ranges. Figure 2 shows typical spectra with spectral types estimated from $(V\text{-}K)_0$ (Kenyon & Hartmann, 1995). Despite care taken with sky subtraction, lower SNR spectra show residual sky lines which could adversely effect $v \sin i$ measurements if not masked prior to further analysis. A total of 411 spectra

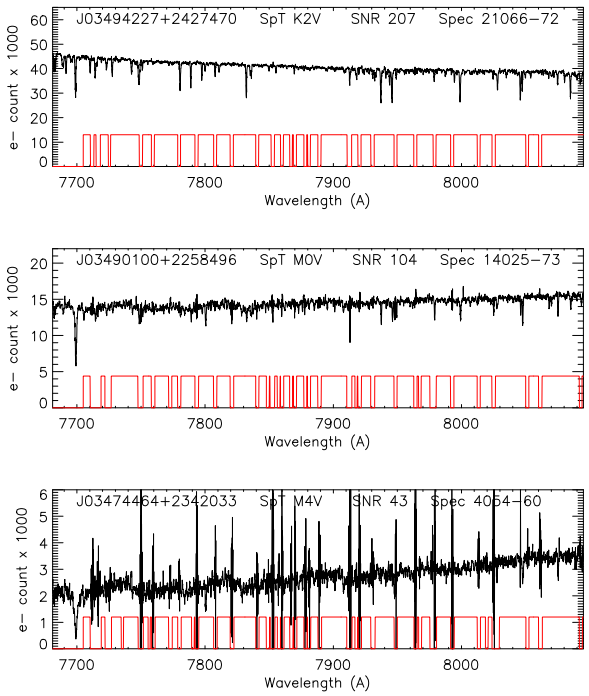

Figure 2. Representative spectra of stars in the Pleiades showing the presence of skylines in lower SNR spectra. The spectral types (SpT) shown are estimated from $(V\text{-}K)_0$ using the relationship proposed by Kenyon & Hartmann (1995). The lower (red) plots indicate sections of the spectra that are masked to minimise the effect of sky lines for measurement of RV and $v \sin i$.

were collected for 324 separate targets in the Pleiades. 10 spectra were rejected from further analysis because of a low SNR ($\leqslant 9$) reducing the number of Pleiades targets to 319.

3.2 Measurement of radial velocities and spectral broadening

RV and $v \sin i$ were measured by cross correlating the median spectra of individual targets with the spectra of standard stars and then fitting a Gaussian function to characterise the peak in the cross-correlation function (CCF). RVs were determined from the position of the peak in the CCF and the spectral broadening was estimated from the increase in full width half maximum (FWHM) of the Gaussian fit with respect to FWHM_0, the CCF FWHM measured for slow-rotating stars of similar spectral type.

For this analysis the spectra were truncated shortward of 7705Å to avoid strong telluric features. Spectra were also masked at the positions of the strong skylines (see Fig. 2) and rebinned (with 10000 points) on a logarithmic wavelength scale, The masked spectra were cross-correlated with template spectra taken from the UVES atlas (Bagnulo et al. 2003). Five templates were used to approximately match the expected spectral types of Pleiades targets based on their (binned) absolute K magnitude (see Table 3). Cross-correlation yielded RV and FWHM values for 319 targets, but 5 of these were rejected after visual inspection; 2 were well-separated spectroscopic binaries and 3 had very poor Gaussian fits to the peaks in their CCFs.

Table 3. Calibration standards. Target spectra are cross correlated with spectra of CCF templates (see section 3.2). Spectra of $v \sin i$ standard stars are used to define calibration curves of $v \sin i$ versus FWHM (see section 3.3).

No.	M_K range	CCF template (spectral type)	$v \sin i$ standard(s)
1	>5.5	HD 34055 (M6V)	Gl 133/Gl 285
2	4.9 - 5.5	HD 130328 (M3III)	Gl 133/Gl 285
3	4.4 - 4.9	HD 156274 (M0V)	Gl 184/Gl 205
4	3.9 - 4.4	HD 10361 (K5V)	Gl 184/Gl 205

3.3 Measurement precision

The precision of RV and FWHM measurements were determined empirically from the change in RV and FWHM between repeated measurements of the same target either in the same configuration (1a and 1b in Table 1) or for targets present in two or more configurations. To maximise the sample size, targets from Praesepe (see section 2.3) were also included in the analysis to give a total of 174 repeats compared with 65 in the Pleiades alone. Assuming that the standard deviation of the measurements of both RV and $v \sin i$ are proportional to the FWHM of the CCF, the distribution of measurement uncertainties measurement was characterised by a t-distribution, with ν degrees of freedom, with a width that is scaled by a function that features a fixed systematic component plus a component that depends on SNR. In the limit of $\nu \rightarrow \infty$ this would be equivalent to a Gaussian with a standard deviation given by the scaling function.

Uncertainties were estimated from repeat observations of individual targets (E_{RV}=$\Delta RV/\sqrt{2}$ and E_{FWHM}=ΔFWHM/$\sqrt{2}$). The distributions of these were modelled in order to choose an appropriate ν and to obtain empirical values for the dimensionless parameters, A,B,α and β of the scaling functions S_{RV} and S_{FWHM}, where S in each case is a measure of the standard deviation and defined as

$$S_{RV} = \mathrm{FWHM}\sqrt{\mathrm{A}^2 + (\mathrm{B}/\mathrm{SNR})^2}\,, \quad (2)$$

where $A = 0.025$ and $B = 0.95$, and

$$S_{\mathrm{FWHM}} = \mathrm{FWHM}\sqrt{\alpha^2 + (\beta/\mathrm{SNR})^2}\,, \quad (3)$$

where $\alpha = 0.036$ and $\beta = 0.68$. Given that the FWHM is $\geqslant 22$ km s^{-1}, this indicates absolute uncertainties in RV of at least 0.5 km s^{-1} and FWHM uncertainties of at least 0.8 km s^{-1}, once the SNR greatly exceeds ~ 40.

The upper plot in Fig. 3 shows the cumulative distribution of the normalised uncertainty in RV (i.e the ratio of measured uncertainty to the uncertainty predicted by S_{RV} using the best fit values of A and B. A t-distribution with $\nu = 4$ degrees of freedom is a good match to the data. Note that a finite value of ν indicates that the tails of the distribution are more prominent than a normal distribution and that a 68.3 per cent confidence interval would be given by $1.14\,S_{RV}$ for $\nu = 4$. The lower plot shows the distribution of normalised measurement precision for FWHM. In this case the tail of the normalised distribution is slightly more extended such that a t-distribution with $\nu = 3$ provides a better fit and a 68.3 per cent confidence error bar would be given by $1.20\,S_{\mathrm{FWHM}}$.

3.4 RV and $v \sin i$ for the Pleiades targets

Table 4 gives the measured RV and FWHM and estimated uncertainties of the 314 Pleiades targets with well defined CCFs that can

Table 4. Measured values of relative RV, FWHM, $v \sin i$ and $R \sin i$. When the relative uncertainty in $v \sin i$ is greater than 30 per cent an upper limit of $v \sin i$ is shown based on the measurement uncertainty in FWHM (see section 3.4.3). The corresponding upper limit in $R \sin i$ is treated as left-censored data in the maximum likelihood analysis determination of over-radius. A sample of the Table is shown here, the full version is available electronically.

Target name (as 2MASS)	M_K (mag)	$\log L/L_\odot$	Period (d)	SNR	RV (km/s)	S_{RV} (km/s)	FWHM (km/s)	$S_{\rm FWHM}$ (km/s)	FWHM$_0$ (km/s)	$v \sin i$ (km/s)	$S_{v \sin i}$ (km/s)	$R \sin i$ ($R_\odot$)
J03414895+2303235	7.51	-2.26	0.239	9.9	-1.2	2.9	29.2	2.3	24.2	18.2	4.1	0.087
J03415671+2358434	7.57	-2.27	0.401	15.9	0.7	2.4	37.6	2.1	24.2	28.4	2.2	0.228
J03415864+2257020	6.22	-1.68	6.842	36.3	-1.2	0.9	24.7	1.0	24.2	$<$10.6	—	$<$1.44
J03421789+2406578	7.29	-2.15	0.603	47.7	0.1	0.9	26.9	1.0	24.2	13.2	2.5	0.159
J03422626+2351386	7.77	-2.36	0.496	13.7	-1.1	1.9	25.4	1.6	24.2	$<$12.8	—	$<$0.13
J03422941+2247261	5.24	-1.25	0.325	73.7	3.1	2.1	74.8	2.8	24.7	50.8	1.4	0.330
J03423396+2411008	7.74	-2.34	0.564	28.5	-0.5	1.2	27.9	1.2	24.2	15.9	2.6	0.179
J03424184+2400158	7.00	-2.01	0.671	65.3	-0.5	0.9	30.4	1.1	24.2	20.2	1.9	0.271
J03424239+2320218	5.77	-1.53	0.269	45.7	0.6	1.1	33.4	1.3	24.2	23.8	1.7	0.128

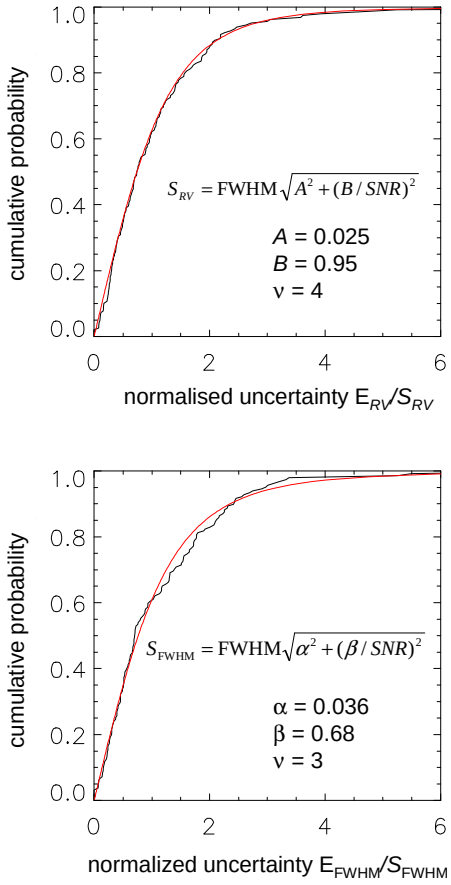

Figure 3. Measurement precision of RV and FWHM estimated from the the CCF with template field stars (see Table 3): Plots shows the cumulative distribution functions of the uncertainties (normalised using equations 2 and 3 with the parameters shown on the plots).

be used to determine stellar $v \sin i$. Where repeated measurements were made of the same target the values shown in Table 4 are the weighted (by S^{-2}) mean values.

3.4.1 *Cluster RVs*

The RVs in Table 4 are measured relative to the central RV of the cluster such that $RV_{\rm rel} = RV - RV_0$ where RV_0 is the median value of the target RVs measured relative to a particular CCF standard (see Table 3). The dispersion of the measured $RV_{\rm rel}$, estimated from the median absolute dispersion (MAD) of the target RVs, is σ_t=1.2 km s^{-1} (using the approximate relation σ_t =MAD/0.68 for a t-distribution with $\nu = 4$). σ_t is due to the combined effect of (a) intrinsic dispersion in the cluster, (b) measurement uncertainties and (c) the effects of binarity. It is used here to define a window of acceptable RVs for Pleiades membership as $|RV_{rel}| < 10$ km s^{-1}. Using this criterion eliminates 9 targets as possible non-members or short period binary systems.

3.4.2 *The FWHM zeropoint*

Figure 4 shows FWHM of the CCFs as a function of M_K for the Pleiades targets, with vertical dashed lines showing the absolute magnitude ranges used to decide which templates were used to calculate the CCF. Also shown are the FWHM values for slow-rotating targets in Praesepe (i.e. targets with $(v \sin i)_p < 3$ km s^{-1}). The FWHM of 93 (predicted) slowly rotating Praesepe targets together with 22 similar slow rotators in the Pleiades were used to define the median CCF width for slow-rotating stars, FWHM$_0$, in the respective M_K bins. The relationship between the FWHM$_0$ and M_K is shown in Fig. 4 and given for each star in Table 4.

3.4.3 *$v \sin i$ values and their precision*

The target $v \sin i$ values were determined from ΔFWHM=FWHM-FWHM$_0$ using calibration curves produced by artificially broadening the spectra of bright, slowly rotating standard stars measured at the beginning and end of each observing night. The $v \sin i$ standards used to calibrate each range of M$_K$ are given in the final column of Table 3. The broadening kernel assumed a linear limb darkening coefficient of 0.6 (Claret, Diaz-Cordoves & Gimenez 1995). Figure 5 shows the relationship between $v \sin i$ and ΔFWHM for the range of spectral types in our sample. For values of $v \sin i > 60$ km s^{-1} we found that the exact calibration depended on which template star was chosen, even at the same spectral type. Instead, for these rapid rotators, the relationship was linearly extrapolated from smaller values, which we found provided a good match to the cross-correlation FWHM values obtained from high SNR spectra of slowly rotating Pleiades members of similar absolute magnitude

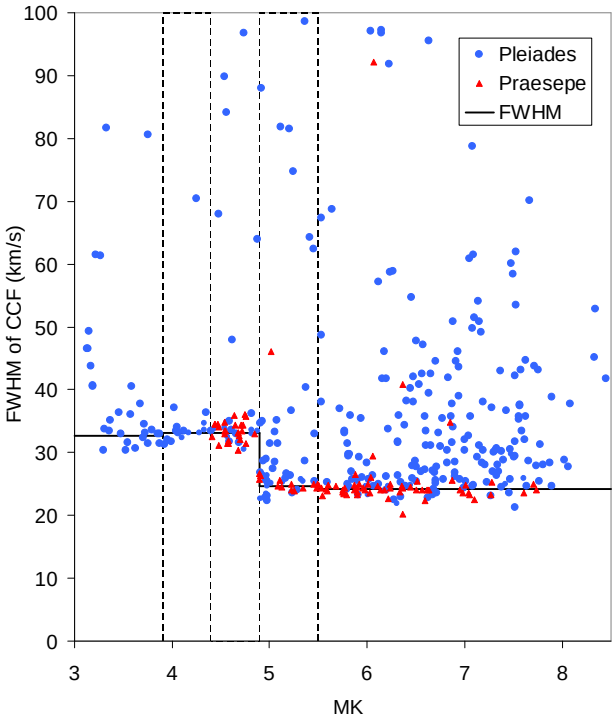

Figure 4. FWHM of the CCF measured on targets in the Pleiades (blue circles) and Praesepe (red triangles) as a function of M_K. Dashed vertical lines delineate the ranges where particular templates were used to calculate the CCF (see Table 3). Horizontal bars show the derived zero-point, FWHM_0, for slow-rotating stars as a function of M_K.

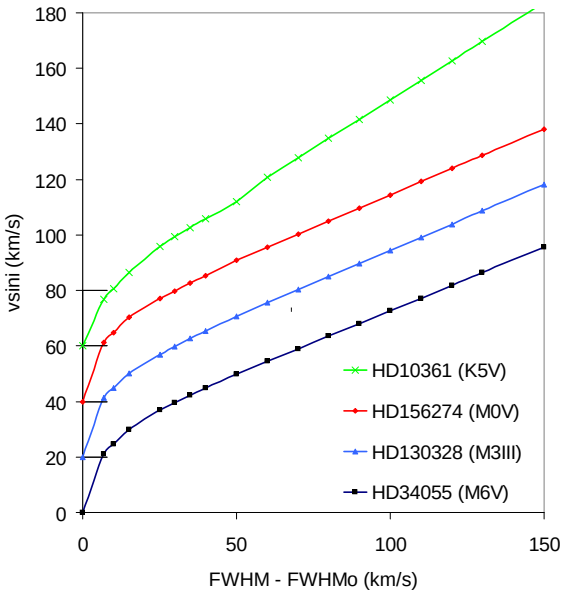

Figure 5. Calibration curves of $v \sin i$ as a function of the FWHM of the CCF. Results are shown for the four CCF templates listed in Table 3 cross correlated with artificially broaded vsini standards of similar spectral type (see section 3.4.3). Curves are offset on the vertical axis in increments of $20\,\mathrm{km\,s^{-1}}$.

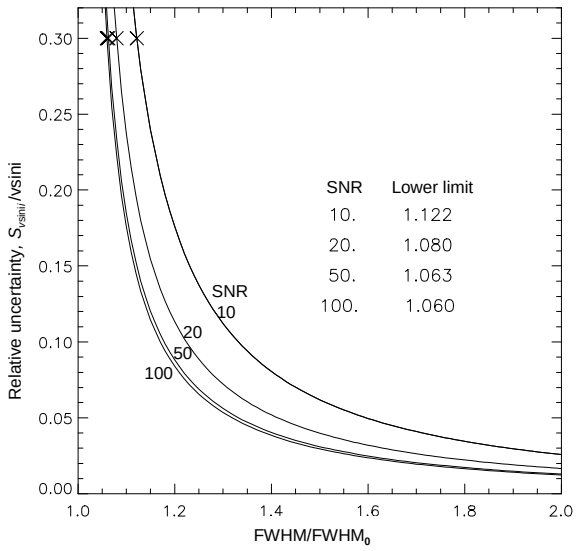

Figure 6. Measurement precision of $v \sin i$. The plot shows shows the relative uncertainty in $S_{v \sin i}/v \sin i$ (see eqn. 4) as a function of the measured FWHM for increasing levels of SNR. Tabulated values on the plot show the minimum levels of $\mathrm{FWHM/FWHM_0}$ at each SNR value that can be discerned to yield a 30 per cent uncertainty in $v \sin i$.

that were artificially broadened. This comparison also reveals that the calibration uncertainties appear to grow from very small values at low $v \sin i$ to $\sim \pm 5$ per cent for $v \sin i \geqslant 70\,\mathrm{km\,s^{-1}}$. However, since fewer than 5 per cent of the sample used to determine the over-radius in Pleiades stars (see section 4) are in this regime, this systematic calibration uncertainty leads to < 1 per cent uncertainty in our final results and we neglect it in the rest of the analyses.

The calibration curves in Fig. 5 vary approximately as $(v \sin i)^2 \propto \Delta\mathrm{FWHM}$ for $v \sin i < 60\,\mathrm{km\,s^{-1}}$ and the precision in $v \sin i$ varies as $S_{v \sin i} = \frac{\partial v \sin i}{\partial \mathrm{FWHM}} S_{\mathrm{FWHM}}$. Using these expressions the *relative* precision in $v \sin i$, defined here as $E_{v \sin i} = \Delta v \sin i/(\sqrt{2} v \sin i)$, scales as

$$\frac{S_{v \sin i}}{v \sin i} \simeq \frac{\sqrt{\alpha^2 + (\beta/SNR)^2}}{2(1 - \mathrm{FWHM_0/FWHM})} \,. \qquad (4)$$

This formulation should be reasonably accurate up to $v \sin i \sim 60$ $\mathrm{km\,s^{-1}}$, but may underestimate the uncertainties for the small number of very fast rotators in our sample. Figure 6 shows the variation of the relative uncertainty in $v \sin i$ with $\mathrm{FWHM/FWHM_0}$ for increasing levels of SNR. These plots were used to calculate the $v \sin i$ uncertainty and also to define a threshold for $\mathrm{FWHM/FWHM_0}$, as a function of SNR, that marks where the level of rotational broadening is large enough to yield a resolved value of $v \sin i$. We choose this threshold such that the relative uncertainty in $v \sin i$ is < 0.3 and targets with $\mathrm{FWHM/FWHM_0}$ below this level are assigned an upper limit value of $v \sin i$ at the value corresponding to this threshold value. The threshold varies from $\mathrm{FWHM/FWHM_0} = 1.12$ for SNR$= 10$ to $\mathrm{FWHM/FWHM_0} = 1.06$ for SNR$= 100$. These threshold FWHM values correspond to $v \sin i$ upper limits of $< 13\,\mathrm{km\,s^{-1}}$ and $< 10\,\mathrm{km\,s^{-1}}$ respectively, with a small dependence on spectral type.

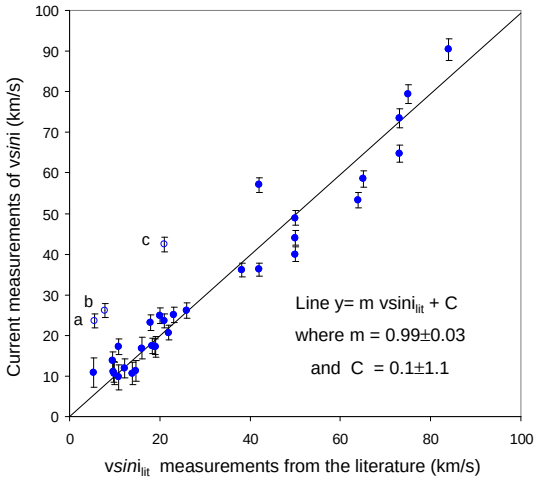

Figure 7. A comparison of $v \sin i$ values (with fractional uncertainties of < 30 per cent and $|RV_{\rm rel}| \leqslant 10\,{\rm km\,s^{-1}}$) with literature values (Queloz et al. 1998, Marilli et al. 1997, Stauffer and Hartmann 1987, Soderblom et al. 1993, O'Dell et al. 1994 and Krishnamurthi et al. 1998). The solid line is a linear regression, neglecting the three outliers J03484894+2416027, J03434841+2511241 and J03475973-2443528 marked as a,b and c respectively on the plot. Error bars are 68 per cent empirical uncertainties in our measurement precision.

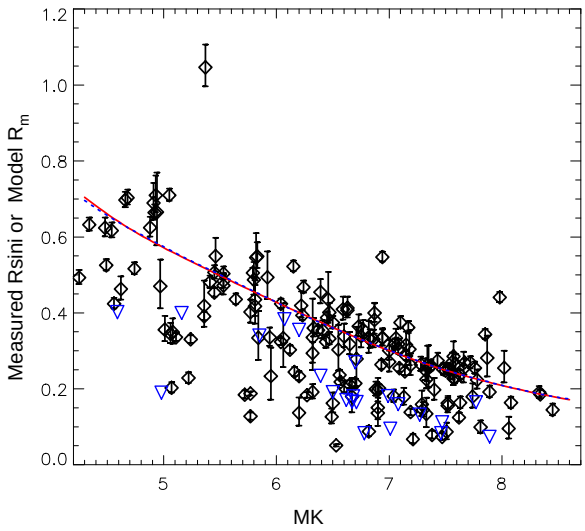

Figure 8. Variation of the projected radii, $R \sin i$ with M_K for Pleiades K- and M-dwarfs. Diamonds with error bars show targets with a relative uncertainty in $R \sin i \leqslant 30$ per cent. Triangles show upper limit values for targets with higher levels of uncertainty. Solid and dashed lines show predicted radii in solar units of the BHAC15 and Dartmouth (Dotter et al. 2008) 120 Myr solar metallicity isochrones.

3.4.4 Comparison of $v \sin i$ with other work

The empirical analysis described above gives only a partial estimate of the absolute accuracy, which is due to both the measurement precision and the uncertainty in the absolute calibration. To assess the calibration accuracy, our values for $v \sin i$ were compared with those reported in the literature. Matches were found for 31 targets with $|RV_{rel}| \leqslant 10\,{\rm km\,s^{-1}}$ and relative uncertainty in $v \sin i \leqslant 0.3$. The comparison is shown in Fig. 7 and demonstrates satisfactory agreement between the two datasets. There are three distinct outliers, two of which, marked (a) and (c) in Fig. 7, are identified as spectroscopic binaries in Mermilliod et al. 1992. Linear regression of the two datasets (excluding the three outliers) shows no significant systematic difference between our $v \sin i$ measurements and the literature values.

4 COMPARISON OF MEASURED RADII WITH CURRENT EVOLUTIONARY MODELS

The measurements of $v \sin i$ in Table 4 are used with the reported rotation periods to estimate projected radii $R \sin i$ (using Eqn. 1) for Pleiades members with $|RV_{\rm rel}| < 10\,{\rm km\,s^{-1}}$. The uncertainty in $R \sin i$ is estimated on the basis that the uncertainty in $v \sin i$ is much greater than the uncertainty in period giving a *fractional* uncertainty in $R \sin i$ of $S_{v \sin i}/v \sin i$, as in Eqn. 4. For targets where this fractional uncertainty is greater than 0.3, we assign upper limits to $R \sin i$ as calculated from the target's period and the upper limit to $v \sin i$.

In the subsequent analyses the sample is restricted to those objects with $(v \sin i)_p > 10\,{\rm km\,s^{-1}}$. This threshold is chosen to approximately match the resolution limit of our measurements of $v \sin i$. Whilst our analyses *do* incorporate upper limits, enlarging the sample to include more slowly rotating stars simply adds many upper limits that do not constrain any over-radius and just add more noise to the results. The reader should then be aware that our radius measurements can only apply to those relatively fast-rotating stars that are in this restricted sample. The effects of increasing the $(v \sin i)_p$ threshold to a more restrictive 15 ${\rm km\,s^{-1}}$ (and decreasing the sample size) has no systematic influence on the results (see section 5.1).

Figure 8 shows $R \sin i$ versus M_K for the restricted sample together with predicted model radii R_m from the BHAC15 and Dartmouth evolutionary codes (Dotter et al. 2008). For practical purposes these two models are identical over the range of the data considered here. In what follows, the ratio of projected radius to model radius at the target luminosity, $r \sin i = R \sin i / R_m$, is referred to as the "normalised radius". In the absence of radius inflation the distribution of $r \sin i$ would simply reflect the values of $\sin i$ in the sample convolved with any measurement uncertainties and biases. Where targets show radius inflation (i.e. $R/R_m > 1$) then the $r \sin i$ distribution would also be scaled by a similar amount.

Fig. 9 recasts Fig. 8 to show $r \sin i$ as a function of $\log L/L_\odot$ for targets with $-2.7 \leqslant \log L/L_\odot \leqslant -0.6$. According to BHAC15 this range of $\log L/L_\odot$ is roughly equivalent to $0.8 \geqslant M/M_\odot \geqslant 0.1$, which spans spectral types of ∼K3 to ∼M5 (Kenyon & Hartmann 1995). There are a total 172 targets with measured values of $r \sin i$ with a relative uncertainty $\leqslant 0.3$. A further 22 targets have only upper limits to their $r \sin i$ and are represented as left censored data in subsequent analyses.

The peak in the distribution *appears* higher than would be expected for stars with a random alignment of spin axes, $\overline{r \sin i} \sim \pi/4$, indicating that the stellar radii may be systematically larger than predicted by the models.

4.1 Maximum likelihood method

A maximum likelihood method is used to determine the average radius ratio or over-radius, $\rho = R/R_m$ of the measured data relative to BHAC15 model radii, as a function of luminosity. The approach is similar to that used by Lanzafame et al. (2017) to estimate the

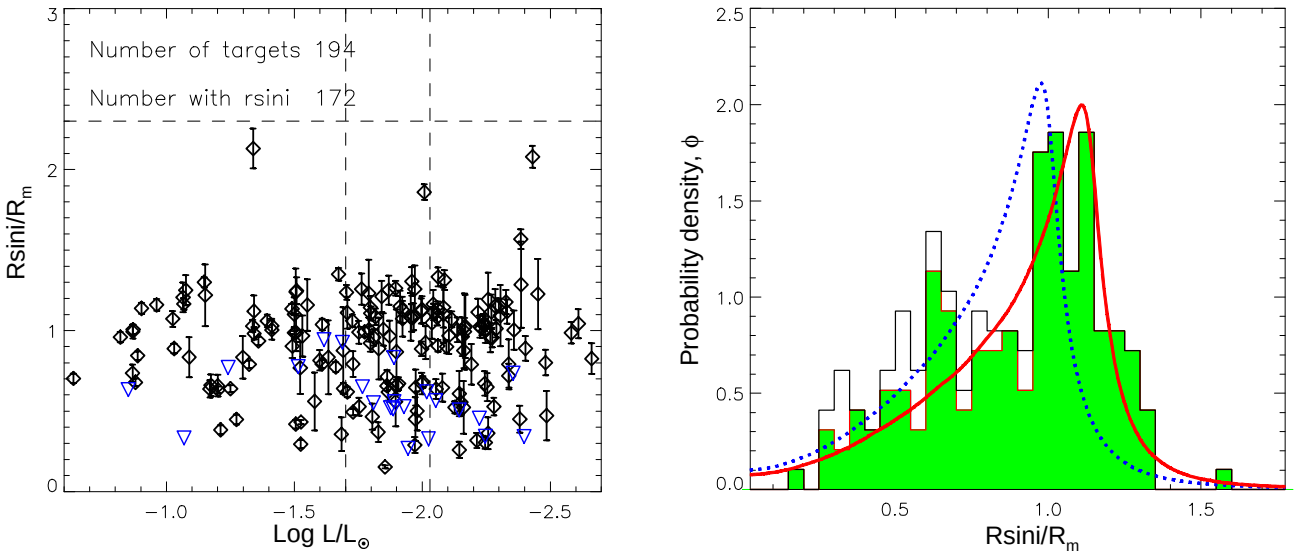

Figure 9. Normalised radii in the Pleiades. Plot A shows $r \sin i$ as a function of luminosity (see Table 2). Diamonds with error bars show $r \sin i$ for targets with a relative uncertainty $\leqslant$30 per cent. Triangles show upper limits for targets $(v \sin i)_p > 10$ km s^{-1} with higher levels of uncertainty ($\geqslant$ 30 per cent). Plot B shows a the number density ($P_{r \sin i}$) of targets with a relative uncertainty $\leqslant$ 30 per cent as a solid histogram, with the open histogram including the stars with upper limits at their upper limit values. The dotted line shows $P_{r \sin i}$ for stars with the radii that are predicted by the BHAC15 evolutionary model (i.e. an over-radius $\rho = 1$). The solid red line shows the maximum likelihood model which corresponds to an average over-radius of $\rho \sim 1.14$ relative to the BHAC15 model.

over-radius of higher mass stars in the Pleiades. In the present case the probability of achieving a particular value of $r \sin i$, written as $\phi(r \sin i | P_j, L_j, \rho)$, is calculated for individual targets depending on their period, P_j, luminosity, L_j, and ρ rather than using uniform probability density function for all targets with measured $r \sin i$.

4.2 Probability function for measured data

In the ideal case of error-free measurements of P and $v \sin i$ for single stars, with a random alignment of their spin axes in space, the probability density increases with inclination as $\phi(i) = \sin i$. Hence the probability density function of $r \sin i$ is

$$\phi(r \sin i | \rho) = \rho \tan[\arcsin(r \sin i / \rho)] \text{ for } r \sin i \leqslant \rho. \quad (5)$$

In practice ϕ is modified by the effects of surface differential rotation, binarity and measurement errors. These effects are investigated in the following subsections and as an example, Figure 10 shows how ϕ would be modified for a representative star of mass, $0.4 M_\odot$, SNR= 50 and $(v \sin i)_p = 20$ km s^{-1}.

4.2.1 Surface differential rotation

Surface differential rotation (SDR) can lead to systematic errors in the estimated radii, because solar-type SDR causes the rate of surface rotation to reduce towards the poles (Krause & Raedler 1980). If the starspots responsible for light curve modulation are distributed over a range of latitudes then the measured rotation rate, Ω_m will be less than the rotation rate at the equator, $\Omega_{\rm eq}$. Reinhold et al. (2013) measured periods for thousands of active stars in the Kepler field. In most cases a second period close to the rotation period was detected which they interpreted as resulting from SDR. For low mass stars they found an average difference in rotation rate of $\Delta\Omega$ = 0.08 radians/day between the two measured periods that was almost independent of measured period and is a small fraction

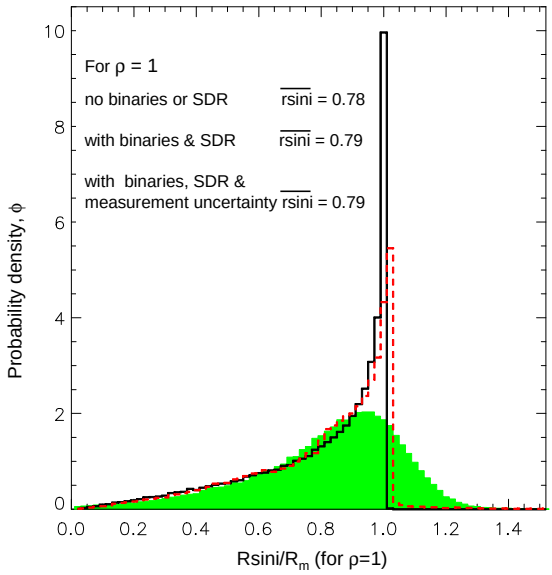

Figure 10. The probability density of measuring a normalised radius $r \sin i$ for a representative star of mass, $0.4\,M_\odot$, SNR= 50 and $(v \sin i)_p = 20$ km s^{-1}. The black line shows the ideal case of precise measurements of P and $v \sin i$ on a single star. The dashed red histogram shows the combined effects of SDR (assumed to increase $r \sin i$ by a fixed 1 per cent, see section 4.2.1) and binarity. The solid green histogram shows the net effect of SDR, binarity and measurement uncertainties.

of the average angular frequency of our Pleiades targets that have a measured $r \sin i$, where $\overline{\Omega_m} = 14$ radians/day. This is in agreement with the analysis of multi-periodic stars in the Pleiades data by Rebull et al. (2016b), where no evidence could be found for

differential rotation among the fast-rotating M-dwarfs that are the subject of this paper. Taking $\Omega_m - \Omega_{eq}$ as *approximately* equal to $\Delta\Omega$ then the fractional increase in measured period compared to the true equatorial period, $\Delta\Omega/\overline{\Omega_m}$ would be $\leqslant 1$ per cent. The corresponding increase in $r \sin i$ will be similarly small.

The potential effects of SDR are shown in Fig. 10 for illustrative purposes, but it is neglected as insignificant in our main analysis and results.

4.2.2 *Binarity*

A proportion of the targets will be part of unresolved binary systems. Short-period binary systems are easily identified from the offset in RV_{rel} from the cluster mean and/or double peaks in their CCF and these are rejected from the sample. However, a fraction of the retained targets will be in longer period spectroscopic binaries, resulting in a broadening and shift in ϕ for two separate reasons, both of which are accounted for with a Monte Carlo simulation of the binary population. We assume a binary frequency for low-mass Pleiades stars of 30 per cent (Duchêne & Kraus 2013). We also adopt the lognormal period distribution and flat mass ratio and eccentricity distributions found for field stars by Raghavan et al. (2010).

First, the CCF may be broadened due to the unresolved velocity difference between the two components. In these cases the measured $v \sin i$ will (on average) be systematically larger than the true $v \sin i$ of the primary star, by an amount that depends on the difference in RV and relative luminosity of the primary and secondary. The effect is modelled as described in Appendix A of Jackson et al. (2016). For each target, the properties of possible secondary stars are drawn at random from the binary distribution described above. The increase in the FWHM of the CCF is then estimated as a function of the line of sight velocity of the primary and secondary stars (relative to the centre of mass) and the relative flux contribution of the secondary at the wavelength of the observed spectra. This is done by measuring the FWHM of a Gaussian profile fitted to the sum of two separate Gaussian profiles representing the primary and secondary stars. The ratio of $v \sin i$ determined from the FWHM of the combined profile to the true $v \sin i$ of the primary is averaged to determine the bias in $v \sin i$ and hence $r \sin i$ caused by binarity. The typical effect is to broaden the distribution of ϕ and produce a small tail of detections with $r \sin i > \rho$. This potential bias in $v \sin i$ decreases with increasing $v \sin i$, but the average effect in our sample is to increase the estimated $r \sin i$ values by an average of < 2 per cent.

Second, the model radius used to calculate $r \sin i$ is systematically over-estimated in binary systems, because the system luminosity is larger than the luminosity of the primary star. This leads to an *under-estimate* of $r \sin i$ if the effect is ignored. For each binary in the simulation we estimate the luminosity of the primary and the system and use this to calculate the bias in $r \sin i$ that is introduced. The average effect for stars in our sample is to decrease the estimated $r \sin i$ values by an average of 3 per cent, and the ϕ distribution is also modified by the appearance of a small "bump" at $r \sin i \sim 0.8$ due to binaries with similar mass components (see Fig. 10).

The net effect of binarity for our sample is to cause a broadening of the ϕ distribution and to decrease the estimated $r \sin i$ by about 1 per cent, although this number will depend linearly on the assumed binary frequency and in a more complex way on the assumed details of the distributions of mass ratio and orbital period. In what follows we will usually neglect the effects of binarity, except where the details of the $r \sin i$ distribution become important in section 5.3.2.

4.2.3 *Measurement uncertainties*

Uncertainties in the measurements will broaden the distribution of ϕ according to the expected fractional uncertainty in $r \sin i$. The uncertainty in P is assumed to be small compared to the uncertainty in $v \sin i$, hence the fractional uncertainty in $r \sin i$ also equals $S_{v \sin i}/v \sin i$. A Monte Carlo method is used to calculate the effect of measurement uncertainties on ϕ, where the fractional uncertainties in trial values of $r \sin i$ are the product of the fractional uncertainty in $v \sin i$ given by Eqn. 4 and random values drawn from a Student's-t distribution with $\nu = 3$. Measurement uncertainties broaden the peak in ϕ but have almost no effect on $\overline{r \sin i}$ (see Fig. 10).

The effects of measurement uncertainties are included in all of our subsequent analyses.

4.2.4 *Multiple periods*

Any uncertainty in P is neglected in our analyses, but in a fraction of cases – 36 of the 194 stars used in the final analysis – Rebull et al. (2016a) report more than one possible period from the Kepler K2 light curves. In all these cases we have used the first period identified by Rebull et al. as P_1, the most likely rotation period of the star. The status and cause of these multiple periods is discussed in detail by Rebull et al. (2016b). For the fast rotating M-dwarfs that constitute most of our sample, the multiple periods are probably due to unresolved binary companions. Given that Rebull et al. (2016a) find very little correlation between photometric amplitude and either rotation period or photometric colour for $V - K > 2$ (which applies to all our targets) then we expect that in the majority of these cases the rotation period reported as P_1 is the rotation period of the brighter primary star and that this corresponds to the $v \sin i$ we have measured. However, there is a possibility that some of these periods are actually the period of an unresolved, fainter secondary star and that the $Pv \sin i$ value is in error.

Without further information we have no way of knowing the probability that the measured period, P_1, is that of the primary star. To test whether this could have any implications for our results we simply repeated the analysis after excluding these stars. The average over-radius (reported in section 5 and see Table 6) inferred from the filtered dataset was increased by 1 per cent, which is smaller than the size of the statistical uncertainties. This small effect is entirely consistent with our earlier assessment of the effect on the $r \sin i$ determination of including unresolved binary systems if P_1 is in fact the period of the brighter primary in all cases.

4.3 Censored data

A probability distribution $\phi(r \sin i | P_j, m_j, \rho)$ is calculated for the $j^{\rm th}$ target. The value of this function at the measured $r \sin i_j$ defines the probability assigned to a particular target, $\phi(r \sin i_j | P_j, m_j, \rho)$. Targets with a relative measurement uncertainty > 0.3 are treated as left censored data where an upper limit $r \sin i_{\rm UL}$ is calculated from the target's period and upper limit to $v \sin i$. The probability density for these stars is estimated as;

$$\phi(r \sin i < r \sin i_{\rm UL} | P_i, m_i, \rho) = \frac{\int_0^{r \sin i_{\rm UL}} \phi(r \sin i | P_i, m_i, \rho)\, d(r \sin i)}{r \sin i_{\rm UL}},$$

(6)

corresponding to the average value of ϕ between 0 and $r \sin i_{\rm UL}$.

4.4 Estimating the best fitting over-radius

The best fit value of ρ is determined by maximising the log-likelihood function;

$$\ln \mathscr{L} = \sum_{l} \ln \phi(r \sin i_j) + \sum_{m} \ln \phi(r \sin i < r \sin i_{{\rm UL},k}) \qquad (7)$$

where $1 \leqslant j \leqslant l$ are the set of targets with measured values of $r \sin i$ and $1 \leqslant k \leqslant m$ are those targets with $r \sin i$ upper limits. The log-likelihood is computed over a range of values of ρ. The maximum of the likelihood-function, $\ln \widehat{\mathscr{L}}$, is used to define the most likely value of ρ, and the standard deviation of the likelihood-function is used to estimate the uncertainty.

5 RESULTS

In this section we present the measured radii of fast rotating low mass stars in the Pleiades relative to the radii predicted for a 120 Myr cluster using BHAC15 evolutionary models. Figure 11 shows the measured period versus luminosity of Pleiades targets with $\log L/L_\odot < -0.2$ reported in Rebull et al. (2016a), Covey et al. (2016) and Hartman et al. (2010), together with those stars for which we obtained spectroscopy and those stars which were included as part of the $r \sin i$ analysis.

5.1 The estimated over-radius

The data were allocated to three luminosity bins for analysis with roughly equal numbers of targets per bin (see Fig. 11). The upper bin spans a relatively wide range of mass (0.4 to 0.8 $M_\odot$, estimated from the BHAC15 models) and includes both fast rotating stars and stars that appear to be in transition between the gyrochronological "C sequence" and slower "I sequence" defined for F-K stars by Barnes (2003, 2007). The central and lower mass bins are more densely populated, but consist of almost exclusively of fast rotating stars. It is clear that the stars included in the $r \sin i$ analysis represent a subset of the total population that is heavily biased towards faster rotators with $P < 2$ days and the majority with $P < 1$ day. It is the radius of these faster rotating stars that is reported here.

The results of the maximum likelihood analysis are presented in Figs. 8 and 12 and summarised in Table 5. Figure 12 shows the main result of this paper: the targets considered here have an average over-radius $\rho = 1.138 \pm 0.013$ relative to the radius-luminosity relation predicted by the solar-metallicity evolutionary models of BHAC15 at an age of 120 Myr. Also shown in Fig. 12 are over-radii for the upper, central and lower mass/luminosity bins, where the maximum likelihood analysis has been conducted separately for each bin. The over-radius in each bin is significantly larger than unity, and consistent with the mean over-radius. There is no strong evidence for any variation in the level of over-radius across this luminosity and mass range.

The results in Table 5 assume an age for the Pleiades of 120 Myr, a distance of 136.2 pc and neglect the small effects of surface differential rotation and binarity discussed in section 4.2. Table 6 shows the effects of changing the assumed age and distance or including the effects of SDR and binarity on the calculated over-radius. Varying the assumed age between 80 and 160 Myr gives

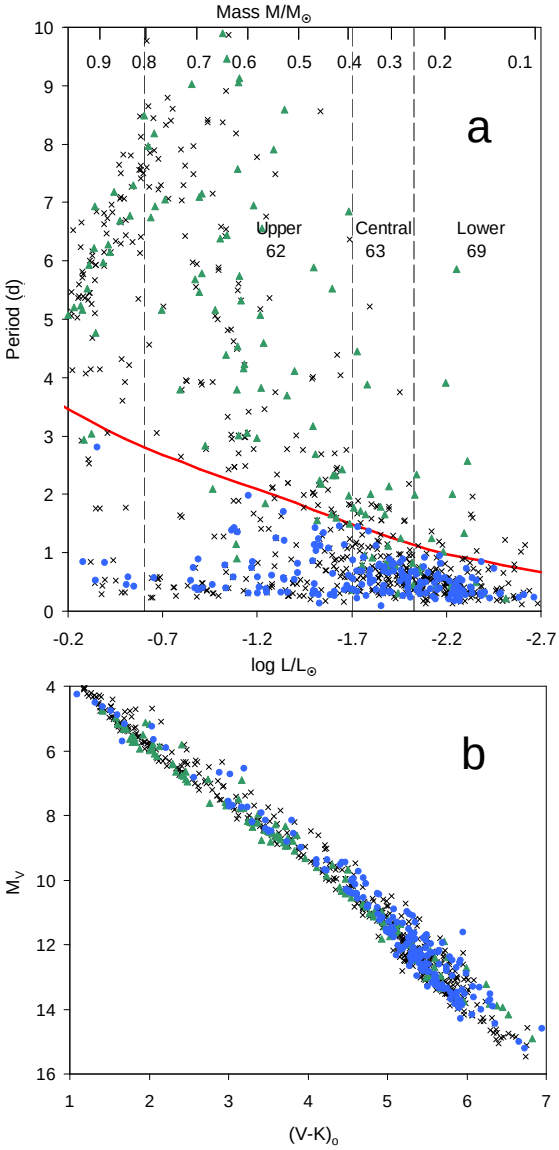

Figure 11. Plot A shows the rotation periods of low mass stars in the Pleiades as a function of luminosity. Circles indicate stars with measured spectra; those circles that are filled are the subset of stars with a measured $r \sin i$ value with uncertainty $\leqslant$ 30 per cent. Crosses show all other stars with measured periods reported by Rebull et al. (2016a), Covey et al. (2016) and Hartman et al. (2010) which were *not* included in our observations. The solid red line marks the locus of stars with $(v \sin i)_p = 10\,{\rm km\,s^{-1}}$; stars below this line are included in the $r \sin i$ analysis. Dashed vertical lines indicate boundaries between the upper, central and lower luminosity bins with numbers indicating the number of $r \sin i$ values bin. Plot B shows the M_V versus $(V-K)_0$ colour magnitude diagram using the same symbols and colour coding.

$1.11 < \rho < 1.14$ (the change in ρ is asymmetric because the stars are already close to the ZAMS at 120 Myr). Altering the distance between 132.6 pc and 140.0 pc (corresponding to the 3σ limits reported by Melis et al. 2014) changes the derived luminosities and hence the predicted radii and gives $1.12 < \rho < 1.16$. The combined effects of SDR and binarity are small, act in opposite directions and depend to some extent on the assumed binary properties of the sample and latitude distribution of spots. The net effect of including these would be only a 1 per cent increase in ρ, but given the

Table 5. The maximum likelihood value of radius ratio, ρ, for faster rotating low mass stars in the Pleiades relative to the radii predicted for a 120 Myr solar metallicity cluster using the BHAC15 evolutionary model. $N_{\rm targ}$ is the number of targets included in the calculation of the likelihood function and $N_{\rm rsini}$ is the number of those targets with measured values of $r \sin i$.

Subset with bins	Bin	$N_{\rm targ}$	$N_{\rm rsini}$	$\log L$	$\overline{r \sin i}$	$\ln \widehat{\mathscr{L}}$	ρ
All targets in bin	All	194	172	-1.823	0.883	-75.3	1.138 ± 0.013
	Lower	69	63	-2.239	0.907	-24.1	1.115 ± 0.028
	Central	63	53	-1.874	0.863	-32.4	1.146 ± 0.033
	Upper	62	56	-1.308	0.876	-19.0	1.151 ± 0.021
Slower rotators	All	106	88	-1.788	0.972	-25.7	1.164 ± 0.024
	Lower	34	30	-2.197	1.000	-5.0	1.166 ± 0.043
	Central	36	28	-1.874	0.991	-10.3	1.192 ± 0.035
	Upper	36	30	-1.315	0.925	-9.5	1.127 ± 0.041
Fast rotators	All	88	84	-1.866	0.790	-49.2	1.121 ± 0.020
	Lower	35	33	-2.281	0.820	-17.4	1.087 ± 0.029
	Central	27	25	-1.875	0.720	-19.4	1.081 ± 0.039
	Upper	26	26	-1.297	0.821	-9.1	1.166 ± 0.034
Lower amplitude light curves	All	98	86	-1.886	0.803	-56.0	1.056 ± 0.022
	Lower	37	33	-2.241	0.833	-16.5	1.063 ± 0.031
	Central	33	28	-1.886	0.751	-25.1	1.057 ± 0.046
	Upper	28	25	-1.415	0.825	-13.5	1.080 ± 0.050
Higher amplitude light curves	All	91	83	-1.795	0.965	-9.2	1.165 ± 0.017
	Lower	32	30	-2.237	0.987	-4.9	1.167 ± 0.038
	Central	29	24	-1.866	0.994	-4.0	1.181 ± 0.037
	Upper	30	29	-1.255	0.920	-0.1	1.165 ± 0.025

Table 6. Sensitivity of the inferred values of the over-radius ρ (overall and in the three luminosity bins introduced in section 5.1), to the assumed age and distance of the cluster and to parameters set in the data reduction pipeline. $N_{\rm targ}$ and $N_{\rm rsini}$ are as defined in Table 5.

		$N_{targ}/$ $N_{r \sin i}$	ρ for bin: Upper	Central	Lower	All	$\Delta\rho^*$
Case 0 -	Reference: age 120 Myr, distance 136.2 pc	194/172	1.15 ± 0.02	1.15 ± 0.03	1.12 ± 0.03	1.138 ± 0.013	—
Case 1 -	Model age reduced to 80Myr	197/173	1.13 ± 0.02	1.11 ± 0.03	1.08 ± 0.03	1.109 ± 0.018	-0.029
Case 2 -	Model age increased to 160Myr	194/172	1.15 ± 0.02	1.16 ± 0.03	1.13 ± 0.03	1.141 ± 0.016	+0.003
Case 3 -	Increased distance distance 140.0 pc	196/173	1.15 ± 0.02	1.11 ± 0.03	1.08 ± 0.03	1.120 ± 0.015	-0.018
Case 4 -	Reduced distance distance 132.4 pc	192/172	1.17 ± 0.02	1.17 ± 0.03	1.13 ± 0.03	1.156 ± 0.015	+0.018
Case 5 -	Compensation for binarity and SDR	194/172	1.16 ± 0.03	1.17 ± 0.03	1.14 ± 0.03	1.152 ± 0.016	+0.014
Case 6 -	Minimum $(v \sin i)_p = 15\,{\rm km\,s^{-1}}$	167/153	1.15 ± 0.02	1.15 ± 0.03	1.11 ± 0.03	1.134 ± 0.014	-0.004
Case 7 -	Excluding targets with multiple periods	158/138	1.17 ± 0.03	1.17 ± 0.03	1.12 ± 0.03	1.150 ± 0.014	+0.012
Case 8 -	Increase value of FWHM_0^{**}	194/166	1.14 ± 0.02	1.12 ± 0.03	1.10 ± 0.03	1.124 ± 0.015	-0.014
	(i) slower rotators	106/83	1.11 ± 0.04	1.17 ± 0.04	1.14 ± 0.05	1.137 ± 0.024	-0.027
	(ii) Faster rotators	88/83	1.16 ± 0.04	1.08 ± 0.04	1.08 ± 0.03	1.117 ± 0.021	-0.004
Case 9 -	Upper 90% of light curve amplitudes	173/158	1.16 ± 0.02	1.16 ± 0.03	1.13 ± 0.03	1.148 ± 0.016	+0.010

* Change in ρ calculated for data over the full luminosity range relative to the reference case.
** The value of FWHM assumed for slow-rotating stars in the calculation of $v \sin i$ is increased by $0.5\,{\rm km\,s^{-1}}$ ($\sim$3 times uncertainty in FWHM_0)

uncertainties we do not include this in our final estimate. Table 6 also shows the effects of excluding stars with multiple periods and of changing the minimum $(v \sin i)_p$ threshold for stars included in the analysis (see section 4). These also lead to only ~ 1 per cent changes in the main results.

Combining expected levels of uncertainties in age and distance with the precision-based uncertainty shown in Table 5 gives a final average over-radius $\rho = 1.14 \pm 0.02$ relative to the solar metallicity BHAC15 model where the uncertainty represents the 68 per cent confidence intervals for an age of 120 ± 20 Myr and a distance of 136 ± 2 pc.

5.2 Comparison of fast and slow rotators and with interferometric radii

In Fig. 13 the over-radius is shown in the three luminosity/mass bins, but now also dividing the stars into faster- and slower-rotating subsamples (note that all these stars should be considered fast rotators when compared with the parent sample of Pleiades stars and that we cannot resolve projected radii for slowly rotating stars in the Pleiades). For the upper and central luminosity bins, the faster rotators are defined as those having with $P < 0.55$ d. For the lower bin the split is made at $P < 0.4$ d and this gives roughly equal numbers of stars in each subsample. Both the central and lower mass bins show a marginal ($\sim 2\sigma$) difference in over-radius between the faster and slower rotators, with the *slower* rotators showing the

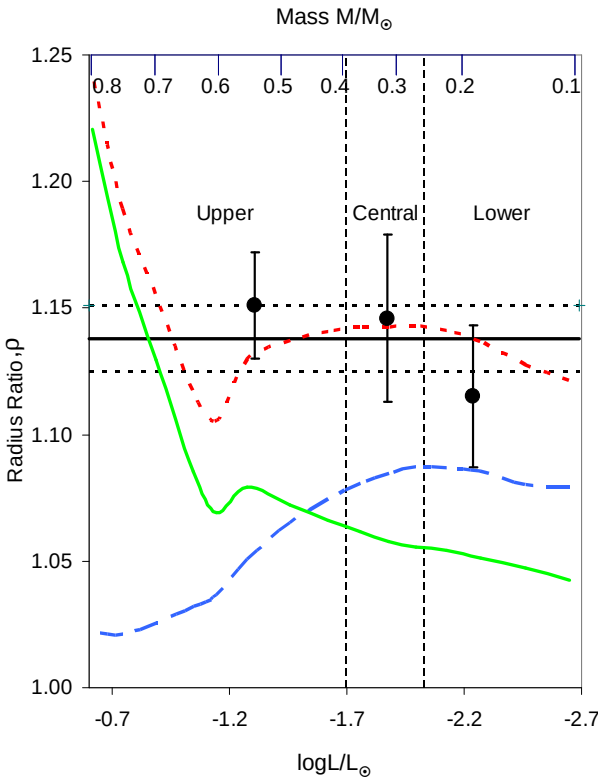

Figure 12. The estimated over-radius for the subsample of Pleiades stars included in the maximum likelihood analysis described in section 4. The over-radius is with respect to the radius predicted by the BHAC15 models for 120 Myr solar metallicity stars at a given luminosity. The horizontal line shows the mean over-radius, for all the data considered, with dashed lines indicating the 1-sigma confidence interval. The individual points with error bars show the estimated mean over-radius and corresponding uncertainties for stars in three luminosity/mass bins. The mass scale at the top of the plot is based on the same BHAC15 model. A green solid line shows the predicted effect of radius inflation due to magnetic inhibition of convection (Feiden et al. 2015); the blue dashed line shows the predicted effect of starpots with an effective dark spot coverage of $\beta = 0.16$ (see section 6.1). The red dotted line shows the combined effect of both magnetic inhibition of convection and starspots with $\beta = 0.16$.

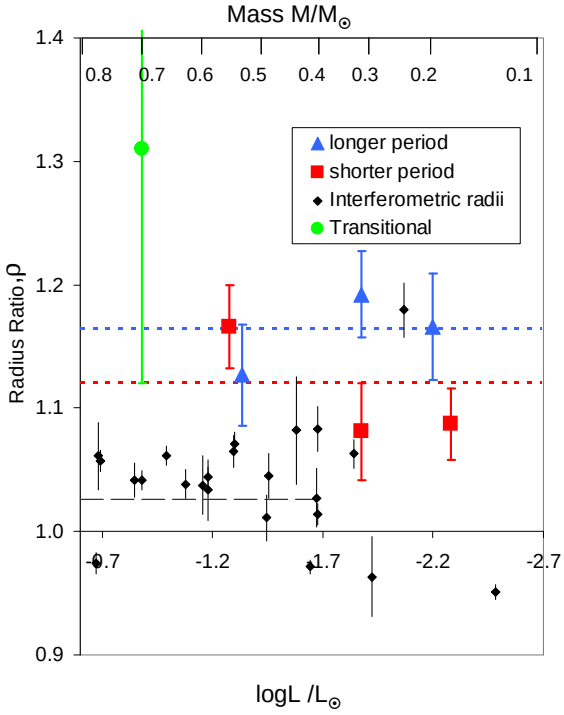

Figure 13. The influence of rotation rate on the over-radius of Pleiades stars relative to the predictions of a BHAC15 120 Myr isochrone. Pleiades targets in each luminosity bin are split by period into faster and slower rotating subsamples (see section 4.5). Also shown are over-radii for low-mass field stars, derived from interferometric radius measurements in Boyajian et al. (2012), and with respect to a 5 Gyr solar-metallicity isochrone from BHAC15. The green point shows a previously reported measurement of ρ for Pleiades stars of $0.6 < M/M_{\odot} < 0.8$ and periods in the transition between the C and I gyrochronological sequences defined by Barnes (2007) ($P >$ 2d, see Table 2 of Lanzafame et al. 2017).

larger over-radius. No significant difference is seen for stars in the upper mass bin.

Figure 13 also shows ρ for individual field stars based on interferometric measurements of stellar radii report by Boyajian et al. (2012) plotted against luminosity values derived from their 2MASS K magnitudes and $V - K$ colours in the same way as the Pleiades data. For these stars, the measured radii are compared to a 5 Gyr solar metallicity BHAC15 isochrone, although neither the age or metallicity are well constrained for most of these targets. There are 19 stars with reported radii in the upper bin, with a weighted mean $\rho = 1.026 \pm 0.007$. The two lower bins contain only 4 stars with significantly scattered normalised radii, so no useful comparison can be made with the models. There is thus evidence for a small over-radius *with respect to the solar metallicity models* for the field M-dwarfs, but it is much smaller than the over-radius found in the Pleiades.

5.3 Biases and selection effects due to spot coverage and the $\sin i$ distribution.

The analysis described above explicitly assumes that the spin axes of targets are randomly distributed in space giving a probability density $\phi(i) = \sin i$. There are a number of reasons why this may not be true: it is easier to resolve $v \sin i$ in targets with higher values of $\sin i$; measurements of period may be biased towards targets with larger $\sin i$ since these would exhibit larger light curve amplitudes due to starspot modulation; or the spin axes may be partially aligned, yielding a bias that could result in either a higher or lower mean $\sin i$ and perhaps a narrowing of the $\sin i$ distribution.

The possibility of bias in the measured over-radius due to the inability to measure $v \sin i$ at low inclinations is already circumvented in the present analysis by explicitly including targets with upper limits in $v \sin i$ as left-censored data. The remaining sources of bias are considered separately below.

5.3.1 *Selection of stars with higher amplitude light curves*

The possibility of bias due to selection effects in the period measurements depends on the completeness of the period data; i.e. whether periods are available for a representative sample of stars, including those with low inclinations. Figure 14 illustrates the potential effect of incomplete sampling of period data on the measured over-radius – selecting stars with higher spot-modulated

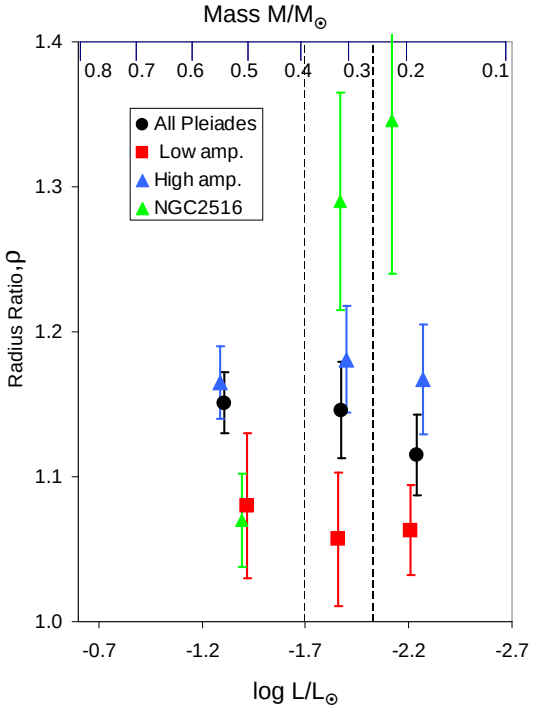

Figure 14. The influence of light curve amplitude on the estimated over-radius. Pleiades targets in each luminosity bin are split into subsamples with higher and lower spot-induced light curve amplitudes (see section 5.3.1). Green triangles show the over-radius of targets in NGC 2516 estimated using previously reported measurements of P and $v \sin i$ (see section 6.2 and Jackson et al. 2010a).

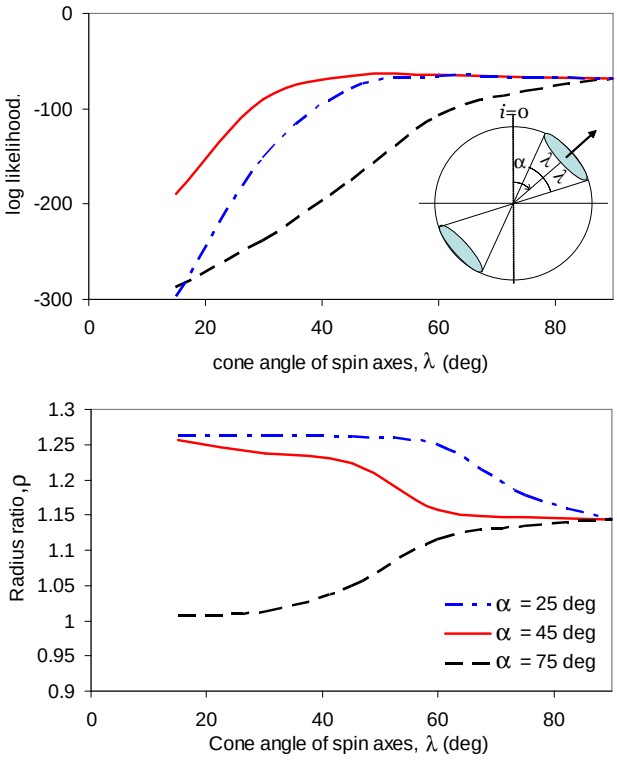

Figure 15. The effect of partial alignment of stellar spin axes. The upper plot shows the variation of $\ln \widehat{\mathscr{L}}$ with cone angle λ, for 3 different values of cone inclination α, relative to the line of sight. The lower plot shows the variation of ρ over the same parameter range

light curve amplitude is expected to preferentially select stars with higher $\sin i$. Selecting for analysis only the 50 per cent of Pleiades targets with the highest light curve amplitude (taken from Rebull et al. 2016a) increases the estimated value of ρ by ~ 3 per cent compared to an analysis of the entire sample. This is actually less than would be expected if light curve amplitude depended solely on $\sin i$, since $\overline{\sin i}$ increases from 0.785 for a randomly distributed sample to 0.96 for a group of objects with $\sin i$ restricted to be above the median of a random distribution.

We do not believe our over-radius results for the Pleiades can be biased by anything like this amount. Most of the targets (189 out of 192) have periods measured from K2 light curves. Rebull et al. (2016a) measured periods for 92 per cent of the Pleiades targets observed. For half of the remaining stars periods were not measured because of non-astrophysical or instrumental effects, leaving just 4 per cent without measured periods that could be Pleiades members with low inclination angles or targets with very long periods or very few (or very symmetrical) star spots.

The effect of missing a small proportion of targets with the lowest amplitude light curves can be assessed by evaluating ρ using only those targets from our list with the top 90 per cent of light curve amplitudes. This produces a small (1 per cent) increase in ρ (see Table 6), indicating that our sample of measured periods, which is complete to ∼96 per cent provides an almost unbiased estimate of ρ.

5.3.2 *Alignment of stellar spin axes*

Jackson and Jeffries (2010a) investigated the effects of partial alignment of spin vectors by modelling cases where spin axes are uniformly distributed inside a cone and zero elsewhere. The cone semi-opening angle, λ, determines the degree of alignment, and the mean inclination of the stars within the cone is α (see Fig. 15). In this case the probability function $\phi(\sin i|\rho)$ in eqn. 5 is replaced by a more complex function, $\phi(\sin i|\rho, \alpha, \lambda)$ calculated using a Monte Carlo method (see eqns. 2 to 6 in Jackson & Jeffries 2010a).

Figure 15 shows the effect of partial alignment of stellar spin axes on the maximum log-likelihood (see Eqn. 7) and the derived value of ρ for $15^\circ < \lambda < 90^\circ$ (the upper limit corresponds to random alignment of the spin axes). In this analysis the effects of SDR and binarity *are* included because whilst they have little effect on the mean inferred $r \sin i$, they *do* have a small, but non-negligible effect on the detailed shape of ϕ. Results are shown for three values of α:

- For $\alpha = 25^\circ$ the spin axes are aligned close to the line of sight, such that the average value of $\sin i$ is lower than the case of a uniform distribution. Consequently a higher value of ρ is required to match the observed set of $r \sin i$ values.
- For $\alpha = 45^\circ$ the spin axes are aligned as shown in the sketch in the upper panel of Fig. 15. If $\lambda < 45^\circ$ then $\overline{\sin i}$ is lower than the uniform case and hence ρ is higher. At larger λ values both the maximum likelihood and ρ are similar to the case of a uniform distribution.
- For $\alpha = 75^\circ$ and small λ the spin axes are aligned almost perpendicularly the line of sight. This both increases $\overline{\sin i}$ and sup-

presses the expected number of targets with low $r \sin i$ (relative to the mean) and therefore provides a poor match to the measured distribution of $r \sin i$. This allows us to say that if α is as large as this, then $\lambda > 80^\circ$ degrees.

6 DISCUSSION

6.1 The over-radius in low-mass Pleiades stars

Observations of low-mass, short-period eclipsing binaries reveal that their components may be inflated by $\sim$10 per cent at a given mass compared with the usual evolutionary models. We have found a similar phenomenon here. The average over-radius in our sample of fast-rotating, low-mass Pleiades stars is 14 ± 2 per cent *at a given luminosity*, which according to the polytropic models discussed by Jackson & Jeffries (2014a), is equivalent to a $\sim$9 per cent over-radius *at a given mass*.

There is no evidence for any mass or luminosity dependence of this over-radius across the range covered by our sample. In particular, we have no evidence that the inflation changes markedly as we move from stars with higher luminosities that have radiative cores, to lower luminosity stars that should be fully convective. For non-inflated stars aged 120 Myr the BHAC15 model shows a radiative core developing at the transition between the central and lower bins in Fig. 12 ($M > 0.3 M_\odot$, $\log L/L_\odot > -2.0$).

It should be stressed that the inferred over-radius is with respect to the evolutionary models of BHAC15 (although the comparison with the models of Dotter et al. 2008 is almost identical). The evolutionary models might fail to correctly predict the measured radii for a number of reasons, although uncertainties in the assumed age and distance are already incorporated into the error bars on the results. Before concluding that the over-radius is due to magnetic activity, as opposed to some other deficiency in the models, we should compare the same models to the measured radii of older, less magnetically active, but otherwise similar stars. The Boyajian et al. (2012) sample of stars with interferometric measurements of angular radii offers this test for the higher mass stars ($>$0.4 $M_\odot$) in our sample (see Fig. 13). Stars in this upper mass bin have a weighted mean over-radius of 2.6 ± 0.7 per cent relative to a 5 Gyr solar metallicity isochrone. Hence the over-radius of the higher mass Pleiades stars relative to the measured radii of inactive field stars of similar luminosity is ~ 10 per cent, although a detailed comparison is hampered by uncertainties in the age and metallicities of the field stars.

Radius inflation at a given luminosity leads to lower effective temperatures and lower core temperatures in contracting PMS stars. Work by Jackson & Jeffries (2014a,b); Somers & Pinsonneault (2015a,b) and Feiden (2016) has considered how this influences the determination of ages and masses of PMS stars in the Hertzsprung-Russell diagram and the onset and rate of lithium depletion in their photospheres as it is burned in the core. The amount of radius inflation we have determined is consistent with what was assumed or modelled in these works and so the consequences will also be similar.

In a cluster like the Pleiades, ages come from either the main-sequence turn-off or the "lithium depletion boundary" (LDB) – the luminosity below which Li is preserved in the interior of a fully convective low-mass PMS star (e.g. Stauffer et al. 1998; Jeffries & Oliveira 2005). The former is unaffected by radius inflation in low-mass stars, but the latter may be. We caution the reader that the LDB in the Pleiades occurs in objects close to the substellar boundary at $\log L/L_\odot \simeq -2.9$ and radius inflation has not yet been established at these low-masses. However, if stars near the LDB were inflated by 14 per cent then the calculations presented by Jackson & Jeffries (2014b; calculated for inflation due to spots, but valid for inflation by any other cause) suggest the LDB age should be increased by 11 per cent, from 125 Myr to 139 Myr.

Somers & Pinsonneault (2015a) and Somers & Stassun (2017) have suggested that inflation varies between roughly zero for the slowest rotators and 15 per cent for the fastest rotators, and could explain the observed rotation-dependent Li depletion pattern in Pleiades K-dwarfs. These stars are at the upper end of the mass range consider here, but the overall level of radius inflation we measure in the fastest rotating cluster members, is in agreement with this hypotheses.

The effects of radius inflation are likely to be even more significant if present at at younger ages. Jeffries et al. (2017) showed, using the example of the Gamma Velorum cluster, that ages inferred from the Hertzsprung-Russell diagram could be doubled by 10 per cent inflation at a given luminosity (slightly less than found here) and that inferred masses would also be significantly underestimated by non-magnetic models, particularly at the lowest stellar masses.

6.1.1 The possible causes of radius inflation

That an over-radius has been observed in the Pleiades whilst the models work reasonably well for older fields stars is circumstantial evidence that magnetic activity and rotation are the factors responsible for the over-radius; although some other age-dependent variation in the physical model could conceivably lead to the observed results.

There are two main "flavours" of magnetic model that might provide an explanation for the observed over-radii - the magnetic inhibition of convection at and just below the surface in layers with significant super-adiabaticity (Feiden & Chaboyer 2012, 2014), or the blocking of radiative flux from the surface of the star by cool, magnetic starspots (Jackson & Jeffries 2014a; Somers & Pinsonneault 2015b). These models predict a different behavior of over-radius as a function of luminosity.

Magnetic inhibition becomes less effective as the convection zone deepens and the stars become fully convective (Feiden et al. 2014). The solid line in Fig. 12 shows the over-radius using the Dartmouth code modified for the effects of magnetic field (Feiden, Jones & Chaboyer 2015) relative to the "standard" Dartmouth model (Dotter et al. 2008), assuming a surface field strength of 2.5 kG as described by Malo et al. (2014). Our results suggests that the magnetic inhibition models, based on an approximate equipartition magnetic field strength at the stellar surface do not inflate the low luminosity stars in our sample sufficiently (by a factor of two).

Conversely, the effect of a given coverage of starspots becomes larger in fully convective stars (Spruit & Weiss 1986). Fang et al. (2016) used the TiO band strengths measured in LAMOST spectra to estimate the spot coverage and temperatures of low mass stars in the Pleiades. Their results can be used to estimate an "effective spot coverage", β, defined as the fraction of stellar flux blocked by starspots compared to the flux of an immaculate photosphere (equivalent to $f_s{}'$ in Fig. 11 of Fang et al.). Comparing target lists we find 22 stars analysed by Fang. et al. with a measured $r \sin i$ in our analysis. The average value of β is 0.16, with a dispersion of 0.09. This can be used to model the effects of spot coverage on the *average* stellar radii (Spruit 1982). The dashed line in Fig. 12 shows the predicted radius ratio for $\beta = 0.16$ as a function of $\log L$, estimated from a linear interpolation of the calculations of

Somers & Pinsonneault (2015a), that use a version of the YREC evolutionary code (van Saders & Pinsonneault 2012) modified to include starspots. If radius inflation were caused *solely* by starspots then this would require $\beta \simeq 0.3$ for the higher mass stars in our sample, decreasing to $\beta = 0.2$ at lower masses where the effects of a given spot coverage are stronger.

These spot coverages are only a little larger than suggested by Fang et al. (2016) but it is possible that β has been underestimated by their simple two-component modelling of the optical spectra. Alternatively, one could have both mechanisms in operation, with the more modest *average* spot coverage measured by Fang et al. (2016) ($\beta = 0.16$) plus magnetic inhibition of convection by an equipartition surface magnetic field (~ 2.5 kG), and the sum of these two would match the measured over-radii reasonably well (dotted line in Fig. 12).

6.1.2 Influence of rotation rate

Given that we are hypothesising that strong, dynamo-induced, magnetic fields are the root cause of the over-radius, it is interesting to investigate whether there is any dependence on rotation rate. Lanzafame et al. (2017) found a complex behavior in Pleiades K-stars and suggested, albeit with low number statistics, that stars with intermediate rotation rates (those between the C- and I-sequences described by Barnes) had larger over-radii than stars with the fastest rotation rates. By splitting our sample into fast and slow(er) rotating halves we have found marginal evidence (see Fig. 13) that partially supports Lanzafame et al.'s result – though we note (i) that our sample does not contain many stars rotating as slowly as those included in Lanzafame et al.'s sample and (ii) that there is no suggestion of separate C- and I-sequences in the rotation period data of lower mass stars ($M < 0.6 M_{\odot}$) in the Pleiades (see Fig. 11). The slow(er) sample has a mean over-radius about 2-sigma higher than the fastest rotators, though note that all of these stars rotate fast enough to be considered magnetically saturated.

It is possible that this difference is linked to the structure of the star and possibly the presence of a radiative core. When considered in three luminosity bins (Fig. 13), our results suggest that any difference in over-radius is confined only to the lowest luminosity stars and in fact there is no significant difference for the high luminosity end of our sample where there is overlap with the sample considered by Lanzafame et al. (2016).

We would caution against ascribing too much significance to this result at this stage, since the samples may be affected by analysis biases that could separate the over-radii of fast- and slow(er)-rotators. For example we are not able to measure $v \sin i$ on slowly rotating targets. Whilst we have taken steps to address this bias in our analysis it is possible that some uncertainties remain. There is also the possibility of uncertainty in the zero-point of the $v \sin i$ calibration. As pointed out by Hartman et al. (2010), if the zero-point is too low then this could result in a significant over-estimate of $v \sin i$ (and hence $r \sin i$) for stars with the smallest resolvable $v \sin i$, but much less effect for the fastest rotators. To test this, we artificially raised the zeropoint by 0.5 km s^{-1}, which is far beyond any likely statistical error in our zero-point (see Table 6). This reduces the overall level of inflation by 1 per cent for the entire sample whilst decreasing the "gap" between faster and slower rotators by 2 per cent.

A more intriguing possibility is that this difference is real. Reiners & Mohanty (2012) have claimed that the angular momentum loss rate due to a magnetically coupled wind is much more strongly dependent on the stellar radius ($\propto R^{16/3}$) than assumed in previous work (e.g. Kawaler et al. 1988) and more strongly than it depends on rotation rate ($\propto \Omega$ in the magnetically saturated regime, which all our stars are). From this perspective, two similar stars with radii that differ by 10–20 per cent would have quite different angular momentum loss rates. Even if greater radius inflation were initially caused by more rapid rotation and greater magnetic activity, the consequent spin-down timescale could be much shorter than the thermal timescale on which an inflated star could react to a slower rotation rate and so we might expect to see that the stars that have begun to spin down are indeed those with larger radii. A more detailed analysis of this possibility is beyond the scope of this paper and perhaps not yet warranted by the quality of the data.

6.2 The discrepancy with NGC 2516

In Jackson et al. (2009) we undertook a similar analysis of spectra for low-mass stars with known rotation period in NGC 2516 - a cluster with a similar age and metallicity to the Pleiades. The results differed in that the deduced over-radius at the lowest masses considered in that paper ($\simeq 0.25 M_{\odot}$) reached ~ 40 per cent. Stars with higher masses were in reasonable agreement with what we find for similar stars in the Pleiades.

Here, we have adopted a maximum likelihood technique including stars with upper limits in $v \sin i$ as left censored data. In the NGC 2516 work, we gave equal weight to each measured $r \sin i$ value and allowed for left-censored data by adopting a lower cut-off in $\sin i$, below which $r \sin i$ could not be measured. Re-running the NGC 2516 dataset through the current analysis pipeline (and also using the BCAH15 models as our baseline), we instead find $\rho = 1.31 \pm 0.06$ for data in the two lower luminosity bins (see Fig. 14). This value of ρ is still significantly higher than the average over-radius measured from Pleiades data.

A substantial and pertinent difference between the Pleiades and NGC 2516 datasets is the fraction of observed targets with measured rotation periods. Jackson and Jeffries (2012) reported that less than half of the NGC 2516 members monitored (from the ground) by Irwin et al. (2007) had subsequently derived rotation periods. This fraction was about 50 per cent in the higher mass bins, dropping to 30 per cent for the lowest luminosity bin. Selecting a similar subset of Pleiades targets, (those with the top 40 per cent of light curve amplitudes in Rebull et al. 2016a) yields $\rho = 1.18 \pm 0.04$ for stars with $M/M_{\odot} < 0.40$. Whilst this is 4 per cent higher than obtained using the full range of amplitudes it is still 13 ± 7 per cent lower than found for similar NGC 2516 targets. We have been unable to identify any other significant systematic differences between the two data sets that might account for this remaining discrepancy, if indeed it is real.

This comparison has highlighted the importance of having as near complete a set of period data as possible when estimating ρ. Whilst the maximum likelihood method used here includes targets with low $v \sin i$ as left censored data it neglects targets without measured periods and this can lead to a bias in the $\sin i$ distribution. Details of cluster members *without* measured periods are often not reported in catalogues of rotation periods and this fraction can be high, especially for ground-based surveys with limited sensitivity to low-amplitude modulation.

6.3 The $\sin i$ distribution

Corsaro et al. (2017) used asteroseismology-based estimates of inclination angles to claim that the distribution of spin-axis vectors

is not random among stars with $M > M_{\odot}$ in two old open clusters in the main Kepler field. They attribute the strong alignment effect they find to the formation of these clusters from a collapsing cloud with a high ratio of rotational to turbulent kinetic energy and the inheritance of some of this angular momentum by the forming stars, especially those with higher masses. From their simulations, Corsaro et al. suggest that this effect may be much weaker in the lower mass stars ($< 0.7 M_{\odot}$) that constitute most of our Pleiades sample. If we assume that the dispersion in $r \sin i$ that we see is mostly caused by a variation in $\sin i$ and not by a star-to-star variation in over-radius, then our observations put constraints on how narrow the distribution of $\sin i$ could be.

Figure 15 showed the effects of alignment of spin axes on $\ln \widehat{\mathscr{L}}$ and ρ when spin axes are uniformly distributed over a cone with half opening angle λ and average inclination α relative to the line of sight (see section 5.3.2). There is no strong evidence of preferential alignment. A model with $\lambda = 90^{\circ}$, equivalent to a random distribution, has $\ln \widehat{\mathscr{L}}$ that is not significantly lower than the best fitting model with $\lambda < 90^{\circ}$ according to the Bayesian information criterion (BIC; $\Delta \mathrm{BIC} \sim 4$). The minimum cone angle that provides a similar value of $\ln \widehat{\mathscr{L}}$ to a random distribution of spin axes is $\lambda \geqslant 30^{\circ}$ if $\alpha < 45^{\circ}$ i.e. a strongly aligned spin axis distribution with $\lambda < 30^{\circ}$ does not match the measured distribution of $r \sin i$ for any mean inclination. If $\alpha > 45^{\circ}$, which is > 70 per cent likely for a randomly distributed α, then the lower limit to λ becomes much larger.

Although the measured distribution of $r \sin i$ could be matched by a partial alignment of spin axes with $\lambda \geqslant 30^{\circ}$, the most likely value of ρ in those cases is always similar to, or larger than, the value obtained by assuming a random distribution of spin axes (see Fig. 15). Thus the mean over-radius of 14 per cent shown in Fig. 12 and Table 5 is the *minimum* that provides an acceptable fit to the measured data.

7 SUMMARY

Precise measurements of rotation periods from the Kepler K2 survey of the Pleiades have been combined with new, precise measurements of rotational broadening for the same stars, in order to estimate their projected radii. Using a maximum likelihood analysis technique and assuming random spin-axis orientation, the average radius of fast-rotating ($P \sim 2$ days or less), low-mass ($0.1 \leqslant M/M_{\odot} \leqslant 0.8$) Pleiades members is 14 ± 2 per cent larger than predicted for stars of the same luminosity by the solar-metallicity Baraffe et al. (2015) and Dotter et al. (2008) models for an assumed age of 120 Myr. The analysis considered unresolved binarity, differential rotation and biases due to the difficulty of measuring rotational broadening for low inclination objects, but these are unlikely to change the results by more than 1-2 per cent. The quoted uncertainties include the statistical precision, which is dominant, and also contributions that account for any plausible uncertainty in the cluster distance and age.

The distribution of projected radius in these low-mass Pleiades stars is consistent with a random orientation of spin axes and is inconsistent with strong alignments where the spin-axis vectors are confined to cones with semi-opening angle $< 30^{\circ}$. Weaker alignments are possible if the mean inclination angle is $\leqslant 45^{\circ}$, but these scenarios would lead to a larger inferred over-radius.

There is no evidence that the radius inflation with respect to model predictions varies over the luminosity range considered (approximately $-0.7 \geqslant \log L/L_{\odot} \geqslant -2.7$) and in particular, no evidence for a change for PMS stars that are fully convective. The same models do predict radii that reasonably match the interferometrically measured radii of older, magnetically inactive field stars with masses and luminosities in the upper half of this range, which is circumstantial evidence that magnetic activity or rapid rotation are the factors responsible. A comparison with existing "magnetic models" suggests that neither magnetic inhibition of convection or flux blocking by starspots can solely explain the over-radius at the expected levels of surface magnetic field or spot coverage, however a simple combination of the two effects does match the data quite well. One remaining puzzle is that although all the stars we consider are very fast-rotating and likely to have saturated levels of magnetic activity, there is evidence that it is the slowest rotating half of this sample that have the largest over-radii.

That low-mass, active stars have larger radii at a given luminosity than predicted by the most commonly used evolutionary models has several important implications. Effective temperatures would be lower; ages derived using the Hertzsprung-Russell diagram and non-magnetic, standard PMS isochrones would be underestimated, as would stellar masses; core temperatures would be lower than expected, leading to delays in the onset of lithium depletion and an extension of the PMS lifetime. The calibration of these effects and the identification of the causes of radius inflation requires careful observation and radius measurements for stars at a range of masses in clusters covering the full range of PMS evolution.

ACKNOWLEDGMENTS

Data presented herein were obtained at the WIYN 3.5m Observatory from telescope time allocated to NN-EXPLORE through (a) the scientific partnership of the National Aeronautics and Space Administration, the National Science Foundation, and the National Optical Astronomy Observatory, and (b) Indiana University's share of time on the WIYN 3.5-m. This work was supported by a NASA WIYN PI Data Award, administered by the NASA Exoplanet Science Institute, though JPL RSA # 1560105. RJJ and RDJ also wish to thank the UK Science and Technology Facilities Council for financial support.

REFERENCES

An D., Terndrup D. M., Pinsonneault M. H., 2007, ApJ, 671, 1640
Bagnulo S., Jehin E., Ledoux C., Cabanac R., Melo C., Gilmozzi R., The ESO Paranal Science Operations Team 2003, The Messenger, 114, 10
Baraffe I., Homeier D., Allard F., Chabrier G., 2015, A&A, 577, A42
Barnes S. A., 2003, ApJ, 586, 464
Barnes S. A., 2007, ApJ, 669, 1167
Bershady M., Barden S., Blanche P.-A., Blanco D., Corson C., Crawford S., Glaspey J., Habraken S., Jacoby G., Keyes J., Knezek P., Lemaire P., Liang M., McDougall E., Poczulp G., Sawyer D., Westfall K., Willmarth D., 2008, in Ground-based and Airborne Instrumentation for Astronomy II Vol. 7014 of PSPIE, WIYN bench upgrade: a revitalized spectrograph. p. 70140H
Boyajian T. S., von Braun K., van Belle G., 2012, ApJ, 757, 112
Carpenter J. M., 2001, AJ, 121, 2851
Claret A., Diaz-Cordoves J., Gimenez A., 1995, A&AS, 114, 247

Corsaro E., Lee Y.-N., García R. A., Hennebelle P., Mathur S., Beck P. G., Mathis S., Stello D., Bouvier J., 2017, Nature Astronomy, 1, 0064
Covey K. R., Agüeros M. A., Law N. M., Liu J., Ahmadi A., Laher R., Levitan D., Sesar B., Surace J., 2016, ApJ, 822, 81
Cummings J. D., Deliyannis C. P., Maderak R. M., Steinhauer A., 2017, AJ, 153, 128
David T. J., Hillenbrand L. A., Cody A. M., Carpenter J. M., Howard A. W., 2016, ApJ, 816, 21
Demory B., Ségransan D., Forveille T., Queloz D., Beuzit J., Delfosse X., di Folco E., Kervella P., Le Bouquin J., Perrier C., Benisty M., Duvert G., Hofmann K., Lopez B., Petrov R., 2009 Vol. 505, Mass-radius relation of low and very low-mass stars revisited with the VLTI. pp 205–215
Dotter A., Chaboyer B., Jevremović D., Kostov V., Baron E., Ferguson J. W., 2008, ApJS, 178, 89
Douglas S. T., Agüeros M. A., Covey K. R., Kraus A., 2017, ApJ, 842, 83
Duchêne G., Bouvier J., Moraux E., Bouy H., Konopacky Q., Ghez A. M., 2013, A&A, 555, A137
Fang X.-S., Zhao G., Zhao J.-K., Chen Y.-Q., Bharat Kumar Y., 2016, MNRAS, 463, 2494
Feiden G. A., 2016, A&A, 593, A99
Feiden G. A., Chaboyer B., 2012, ApJ, 761, 30
Feiden G. A., Chaboyer B., 2014, ApJ, 789, 53
Feiden G. A., Jones J., Chaboyer B., 2015, in van Belle G. T., Harris H. C., eds, 18th Cambridge Workshop on Cool Stars, Stellar Systems, and the Sun Vol. 18 of Cambridge Workshop on Cool Stars, Stellar Systems, and the Sun, Updating the Dartmouth Stellar Evolution Model Grid: Pre-main-sequence Models Magnetic Fields. pp 171–176
Hartman J. D., Bakos G. Á., Kovács G., Noyes R. W., 2010, MNRAS, 408, 475
Horne K., 1986, PASP, 98, 609
Howell S. B., Sobeck C., Haas M., Still M., Barclay T., Mullally F., Troeltzsch J., Aigrain S., Bryson S. T., Caldwell D., Chaplin W. J., Cochran W. D., Huber D., Marcy G. W., Miglio A., Najita J. R., Smith M., Twicken J. D., Fortney J. J., 2014, PASP, 126, 398
Irwin J., Hodgkin S., Aigrain S., Hebb L., Bouvier J., Clarke C., Moraux E., Bramich D. M., 2007, MNRAS, 377, 741
Jackson R. J., Jeffries R. D., 2010a, MNRAS, 402, 1380
Jackson R. J., Jeffries R. D., 2010b, MNRAS, 407, 465
Jackson R. J., Jeffries R. D., 2012, MNRAS, 423, 2966
Jackson R. J., Jeffries R. D., 2014a, MNRAS, 445, 4306
Jackson R. J., Jeffries R. D., 2014b, MNRAS, 441, 2111
Jackson R. J., Jeffries R. D., Maxted P. F. L., 2009, MNRAS, 399, L89
Jackson R. J., Jeffries R. D., Randich S., Bragaglia A., Carraro G., Costado M. T., Flaccomio E., Lanzafame A. C., Lardo C., Monaco L., Morbidelli L., Smiljanic R., Zaggia S., 2016, A&A, 586, A52
Jeffries R. D., 2007, MNRAS, 381, 1169
Jeffries R. D., Jackson R. J., Franciosini E., Randich S., Barrado D., Frasca A., Klutsch A., Lanzafame A. C., Prisinzano L., Sacco G. G., 2017, MNRAS, 464, 1456
Jeffries R. D., Oliveira J. M., 2005, MNRAS, 358, 13
Kamai B. L., Vrba F. J., Stauffer J. R., Stassun K. G., 2014, AJ, 148, 30
Kawaler S. D., 1988, ApJ, 333, 236
Kenyon S. J., Hartmann L., 1995, ApJS, 101, 117
Kraus A. L., Cody A. M., Covey K. R., Rizzuto A. C., Mann A., Ireland M., Jensen E. L. N., Muirhead P. S., 2016, in American Astronomical Society Meeting Abstracts Vol. 227 of American Astronomical Society Meeting Abstracts, The Mass-Radius Relation of Young Stars from K2. p. 236.12
Kraus A. L., Cody A. M., Covey K. R., Rizzuto A. C., Mann A. W., Ireland M. J., 2015, ApJ, 807, 3
Krause F., Raedler K., 1980, Mean-field magnetohydrodynamics and dynamo theory. Pergamon Press, Oxford
Krishnamurthi A., Terndrup D. M., Pinsonneault M. H., Sellgren K., Stauffer J. R., Schild R., Backman D. E., Beisser K. B., Dahari D. B., Dasgupta A., Hagelgans J. T., Seeds M. A., Anand R., Laaksonen B. D., Marschall L. A., Ramseyer T., 1998, ApJ, 493, 914
Lanzafame A. C., Spada F., Distefano E., 2017, A&A, 597, A63
López-Morales M., Ribas I., 2005, ApJ, 631, 1120
MacDonald J., Mullan D. J., 2013, ApJ, 765, 126
Malo L., Doyon R., Feiden G. A., Albert L., Lafrenière D., Artigau É., Gagné J., Riedel A., 2014, ApJ, 792, 37
Marilli E., Catalano S., Frasca A., 1997, Memorie della Societa Astronomica Italiana, 68, 895
Melis C., Reid M. J., Mioduszewski A. J., Stauffer J. R., Bower G. C., 2014, Science, 345, 1029
Mermilliod J.-C., Rosvick J. M., Duquennoy A., Mayor M., 1992, A&A, 265, 513
Messina S., Lanzafame A. C., Feiden G. A., Millward M., Desidera S., Buccino A., Curtis I., Jofré E., Kehusmaa P., Medhi B. J., Monard B., Petrucci R., 2016, A&A, 596, A29
Morales J. C., Ribas I., Jordi C., 2008, A&A, 478, 507
Morales J. C., Ribas I., Jordi C., Torres G., Gallardo J., Guinan E. F., Charbonneau D., Wolf M., Latham D. W., Anglada-Escudé G., Bradstreet D. H., Everett M. E., O'Donovan F. T., Mandushev G., Mathieu R. D., 2009, ApJ, 691, 1400
Mullan D. J., MacDonald J., 2001, ApJ, 559, 353
O'Dell M. A., Hendry M. A., Collier Cameron A., 1994, MNRAS, 268, 181
Pecaut M. J., Mamajek E. E., 2013, ApJS, 208, 9
Queloz D., Allain S., Mermilliod J.-C., Bouvier J., Mayor M., 1998, A& A, 335, 183
Raghavan D., McAlister H. A., Henry T. J., Latham D. W., Marcy G. W., Mason B. D., Gies D. R., White R. J., ten Brummelaar T. A., 2010, ApJS, 190, 1
Rebull L. M., Stauffer J. R., Bouvier J., Cody A. M., Hillenbrand L. A., Soderblom D. R., Valenti J., Barrado D., Bouy H., Ciardi D., Pinsonneault M., 2016, AJ, 152, 113
Rebull L. M., Stauffer J. R., Bouvier J., et al. 2016, AJ, 152, 114
Reiners A., Mohanty S., 2012, ApJ, 746, 43
Reinhold T., Reiners A., Basri G., 2013, A&A, 560, A4
Rhode K. L., Herbst W., Mathieu R. D., 2001, AJ, 122, 3258
Rieke G. H., Lebofsky M. J., 1985, ApJ, 288, 618
Skrutskie M. F., Cutri R. M., Stiening R., Weinberg M. D., Schneider S., Carpenter J. M., Beichman C., Capps R., Chester T., Elias J., Huchra J., 2006, AJ, 131, 1163
Soderblom D. R., Laskar T., Valenti J. A., Stauffer J. R., Rebull L. M., 2009, AJ, 138, 1292
Soderblom D. R., Stauffer J. R., Hudon J. D., Jones B. F., 1993, ApJs, 85, 315
Somers G., Pinsonneault M. H., 2014, ApJ, 790, 72
Somers G., Pinsonneault M. H., 2015a, ApJ, 807, 174
Somers G., Pinsonneault M. H., 2015b, MNRAS, 449, 4131
Somers G., Stassun K. G., 2017, AJ, 153, 101
Spruit H. C., 1982, A&A, 108, 348
Spruit H. C., Weiss A., 1986, A&A, 166, 167

Stauffer J. R., Hartmann L. W., 1987, ApJ, 318, 337
Stauffer J. R., Jones B. F., Backman D., Hartmann L. W., Barrado y Navascués D., Pinsonneault M. H., Terndrup D. M., Muench A. A., 2003, AJ, 126, 833
Stauffer J. R., Schultz G., Kirkpatrick J. D., 1998, ApJ, 499, L199+
Torres G., 2013, Astronomische Nachrichten, 334, 4
van Leeuwen F., 2009, A&A, 497, 209
van Saders J. L., Pinsonneault M. H., 2012, ApJ, 746, 16